Morphology and size of bacterial colonies control anoxic micro-environments formation in porous media

Giulia Ceriotti,*,† Sergey M. Borisov,‡ Jasmine S. Berg,† and Pietro de Anna*,¶

†*Institute of Earth Surface Dynamics, University of Lausanne, Switzerland*

‡*Institute of Analytical Chemistry and Food Chemistry, Graz University of Technology, Austria*

¶*Institute of Earth Sciences, University of Lausanne, Switzerland*

E-mail: giulia.ceriotti@unil.ch; pietro.deanna@unil.ch

Phone: +41 21 692 4423

Abstract

Bacterial metabolisms using electron acceptors other than O_2 (e.g., methanogenesis and fermentation) largely contribute to element cycling and natural contaminant attenuation/mobilization, even in well-oxygenated porous environments, such as shallow aquifers. This paradox is commonly explained by the occurrence of small-scale anoxic micro-environments generated by the coupling of bacterial respiration and the dissolved oxygen (O_2) transport by pore-water. Such micro-environments allow facultative anaerobic bacteria to proliferate in oxic environments. Micro-environments dynamics are still poorly understood due to the challenge of directly observing biomass and O_2 distributions at the micro-scale within an opaque sediment matrix. To overcome these limitations, we integrated a microfluidic device with transparent O_2 planar optical sensors to measure the temporal behavior of dissolved O_2 concentrations and

biomass distributions with time-lapse video-microscopy. Our results reveal that bacterial colony morphology, which is highly variable in flowing porous systems, controls the formation of anoxic micro-environments. We rationalize our observations through a colony-scale Damköhler number comparing dissolved O_2 diffusion and bacterial O_2 uptake rate. Our Damkholer number enables us to predict the pore space fraction occupied by anoxic micro-environments in our system for a given the bacterial organization.

Keywords: Microfluidics, planar sensors, aquifer transport, oxygen, anoxia, porous media, heterogeneity.

Synopsis: Sediments and soils are heterogeneous environments populated by active bacteria. This study explores the coupling of aerobic bacteria respiration and oxygen transport as the key driver for the formation of pore-scale anoxic micro-environments.

Introduction

Although the Earth's atmosphere is well-oxygenated, porous subsurface environments fully or partially saturated by water (such as aquifers, lake/ocean sediments, and soils) are often oxygen (O_2)-limited.[1] Such limitation arises from the low O_2 solubility in water and the porous solid matrix of sediments and soils, constituted by a disordered arrangement of grains, that physically hinders the O_2 diffusion and supply from the external atmosphere.[2–4] As a result, O_2 availability typically decreases with depth, in the subsurface.[5,6]

Since O_2 is the most thermodynamically favorable common electron acceptor, its spatial distribution in the subsurface remarkably influences the activity of the diverse bacteria that populate these natural environments.[2,4] Aerobic respiration is associated with the shallow subsurface that is generally well-oxygenated. Processes using less thermodynamically favorable electron acceptors than O_2 (such as nitrates, iron-oxides, sulfates, and CO_2) are

typically confined to deeper and reducing environments.[4,7,8] Surprisingly, recent investigations have shown the occurrence of non-aerobic metabolisms in well-oxygenated regions of the subsurface.[9–12] For example, oxygenated and well-drained superficial soils largely contribute to methane and NO_X emissions generated by facultative methanotrophs[13] and denitrifiers.[9] Also, Mn reduction and reductive dehalogenation are active processes in oxic aquifers and are crucial players in the natural attenuation and bio-remediation of recalcitrant pollutants that accumulate in groundwater.[14,15]

This apparent paradox results from our limited capacity to fully characterize the pore-scale heterogeneity of the geo-chemical environment experienced by bacteria in the subsurface.[16] Depending on the sampling technique, bulk O_2 measurements typically capture the average oxygenation level over the centimeter-meter scale.[6] Although the bulk system appears well-oxygenated at that scale, pore water may display extremely heterogeneous O_2 distributions over smaller spatial scales ($10\sim1000$ μm)[2] that bacteria directly experience and to which they actively respond.[17,18] At such small scales, diffusion should be very efficient in smoothing O_2 gradients but the tortuous architecture of soils and sediments hinders homogenization by diffusion.[2,10,17,19,20] Pore-water flow (for instance in aquifers and flooded soils), being typically organized in preferential flowing paths and stagnant zones, further contributes to the O_2 heterogeneity.[10,19] Bacteria grow most abundantly along the O_2 and nutrient-rich flow paths[19,21] where they form highly active hotspots.[9] Shear stresses generated by flow and porous geometry,[22,23] in addition to nutrient concentrations and bacterial growth rate,[24] constrain colony sizes and morphology (as thin surface layers, round clusters, clumps, or filaments) which influence colony growth rates and, consequently, O_2 uptake.[25,26]

The formation of local micro-scale zones of low oxygen level, undetected by bulk measurements, may provide micro-habitats for facultative anaerobic bacteria that switch to alternative metabolic pathways other than O_2 respiration.[16] For different facultative strains,

the complete depletion of free O_2 in the environment is not a prerequisite to respire electron acceptors other than O_2, implying that aerobic respiration and alternative facultative metabolisms can occur simultaneously and synergically in these low oxygen level zones.[27,28] Going beyond the strict definition of anoxic as the complete absence of free O_2, we define the local micro-scale low oxygen areas as anoxic micro-environments. These are the zones where facultative anaerobic bacteria might use less thermodynamically favorable electron donors than O_2 for metabolic purposes. These zones are characterized by levels of oxygen that significantly differ from bulk measurements.

Anoxic micro-environments have been observed to occupy no more than 10% of the pore space, are generally smaller than a few millimeters, and persist from hours to days.[4,10,29] Despite the small portion of pore volume occupied, anoxic micro-environments are nowadays considered fundamental to explain the dynamics of many macro-scale ecological processes such as element cycling (e.g., soil carbon stabilization[13] and sulfur reduction and precipitation[30]), greenhouse gas production (e.g., methanogenesis[31,32] and NO_x emissions[17,29,33]), heavy metal mobilization[34,35] and natural attenuation of recalcitrant pollutants that accumulate in groundwater.[14,15]

Yet, a quantitative understanding and predictability of anoxic micro-environments formation in oxic subsurface porous environments is missing due to major methodological limitations. Indeed, direct in-situ monitoring of biomass growth and O_2 distribution at the colony scale remains challenging due to i) the opacity of porous matrices of soils and sediments; and ii) the difficulties in simultaneously capturing the different spatial and temporal scales of interest for anoxic micro-environments formation.[3,9,16] The recent development of luminescent planar sensors,[3,36,37] combined with microscopy, has opened new perspectives enabling the investigation of O_2 spatial distribution at micro-scale resolution. The study of anoxic micro-environments with planar sensors has nevertheless been limited by the use of opaque

sensor foils, which hinder visualization of biomass spatial organization and growth measurements.[4,11,21,34]

To overcome these limitations, we developed an experimental setup that combines transparent O_2 planar sensors with microfluidic devices that reproduce the laminar pore water flow regime through a porous medium, mimicking sandy sediments.[38] With time-lapse automated video-microscopy, we simultaneously monitor bacterial colony growth and O_2 concentrations across the entire porous landscape (covering tens of millimeters with micron resolution) over time, encompassing more than a hundred bacterial generations. Our experimental results provide evidence of the critical role played by the bacterial growth rate and colony morphology in controlling micro-scale O_2 heterogeneity in confined porous systems under laminar flow conditions. To rationalize our observations, we introduce a colony-specific Damköhler number. The latter is computed by comparing the biomass O_2 consumption rate and the O_2 diffusion rate within each individual colony. The so-defined Damköhler number, accounting for bacterial cluster's morphology, can identify the bacterial colonies prone to trigger anoxic micro-environments.

Materials and Methods

Bacterial cultures.

Pseudomonas putida sp. GB1 wild type is a non-motile aerobic soil-dwelling bacterium. Inoculum from frozen stock was grown overnight in 5 mL liquid Luria Bertani (LB) medium at 30°C in an orbital shaker set at 150 rpm. A 100 μL aliquot was resuspended in 5 mL of LB medium and incubated under the same conditions until the early exponential growth stage (i.e., for about 2 hours).

Integration of O_2 planar sensors within porous structures.

We used customized transparent optical sensors to monitor spatial oxygen distribution within the microfluidics device. These sensors rely on a mixture of two luminescent dyes immobilized into a polymeric matrix (polystyrene). The emission of one of the two dyes (Pt(II) porphyrin) is quenched by molecular oxygen whereas the second dye provides a reference signal (see sections S1 and S2 in SI for details). The planar sensor is prepared from a solution of the two dyes, polymer in organic solvent (anisole), that was screen-printed onto a glass slide (25 x 75 mm) and, after solvent evaporation, resulted in a thin layer (below 5 µm) that covered an area of 3 x 27 mm^2. The glass slide supporting this O_2 sensor was integrated into a fully transparent microfluidic device as described in the following.

We designed a two-dimensional porous medium geometry (Figure 1A) composed of non-overlapping disks with varying diameters and centered in random locations. The minimum distance between neighboring grains l_{pt} (referred to as pore-throat) is distributed according to a power law probability density function ($p(l_{pt}) \sim l_{pt}^{-0.08}$). The average pore size is equal to 0.05 mm).[39] The resulting velocity field in porous space is also power law distributed[40] and spans five orders of magnitude, consistently with those observed in natural sediments, e.g., sandstone.[41,42]

Using classical soft lithography, the porous geometry (Figure 1A) was printed onto a microfluidics master with a thickness of $h = 50$ μm (i.e., similar to the average pore-throat size l_{pt}). This was used to mold PDMS chip replicates (Sylgard 184 Silicone Elastomer mixed with 10 w/w % of curing agent; supplier: Dow Corning, Midland, MI). The microfluidic device was assembled by aligning and plasma bonding the PDMS chip to a glass slide previously covered by the optodes (Figure 1B) so that the sensor was in direct contact with the fluid occupying the porous space. The resulting porous system had a length $L = 27$ mm, width $W = 5$ mm, thickness h and porosity $\phi = 0.5$.

Three replicates were prepared by coating the chip's external surface with gas-impermeable NOA-81 glue (Figure 1C) before the experiment. This prevents O_2 diffusion through the PDMS walls from the atmosphere and limits O_2 supply to the inlet flow. Two controls without NOA-81 coating were performed for comparison.

Flow conditions.

Tygon tubing (Cole-Palmer, inner/outer diameter 0.02/0.04 inches) was used to connect the two ends of the microfluidics device (Figure 1B). After degassing, the chip was saturated by injecting the prepared cell suspension through the outlet tube to avoid cell accumulation close to the inlet. After a rest phase of 30 minutes, the inlet tube was replaced with a clean one prior to the injection of a well-oxygenated sterile and nutrient-rich solution (a 10X diluted Luria Bertani broth) for 45 hours at a flow rate of 0.2 μL/min. The resulting Darcy velocity $q = Q/(\phi A)$ was equal to 0.013 mm/s and the Reynolds number (assuming the characteristic length l equal to the pore throat average size $l_{lp} = 0.05$ mm, and kinematic viscosity $\nu = 1$ mm^2/s) was $Re = q\, l/\, \nu \sim 10^{-3}$, corresponding to a laminar flow regime. The Péclet number associated with the O_2 transport is $Pe = q\, l/\, D_m = 0.3$ (where the O_2 diffusion coefficient is $D_m = 2 \cdot 10^{-3}$ mm^2/s) and it indicates a diffusion-limited O_2 transport. The characteristic time necessary for the average flow to displace a fluid volume equivalent to the whole porous system is $t_{PV} = L/q = 33$ min.

Data acquisition.

A fully-automated microscope (inverted Nikon Eclipse Ti-E2) equipped with a 10X objective and an sCMOS camera (Teledyne Phometrics Prime 95B, sensor area 13.2×13.2 mm) captured images of the entire porous landscape in three different optical configurations with a resolution of 1.1 μm/pixel every $\Delta\, t = 1$ hour.

The first optical configuration is an adjusted phase-contrast[18] to monitor the biomass distribution within the chip. The second and third optical configurations capture, separately, the

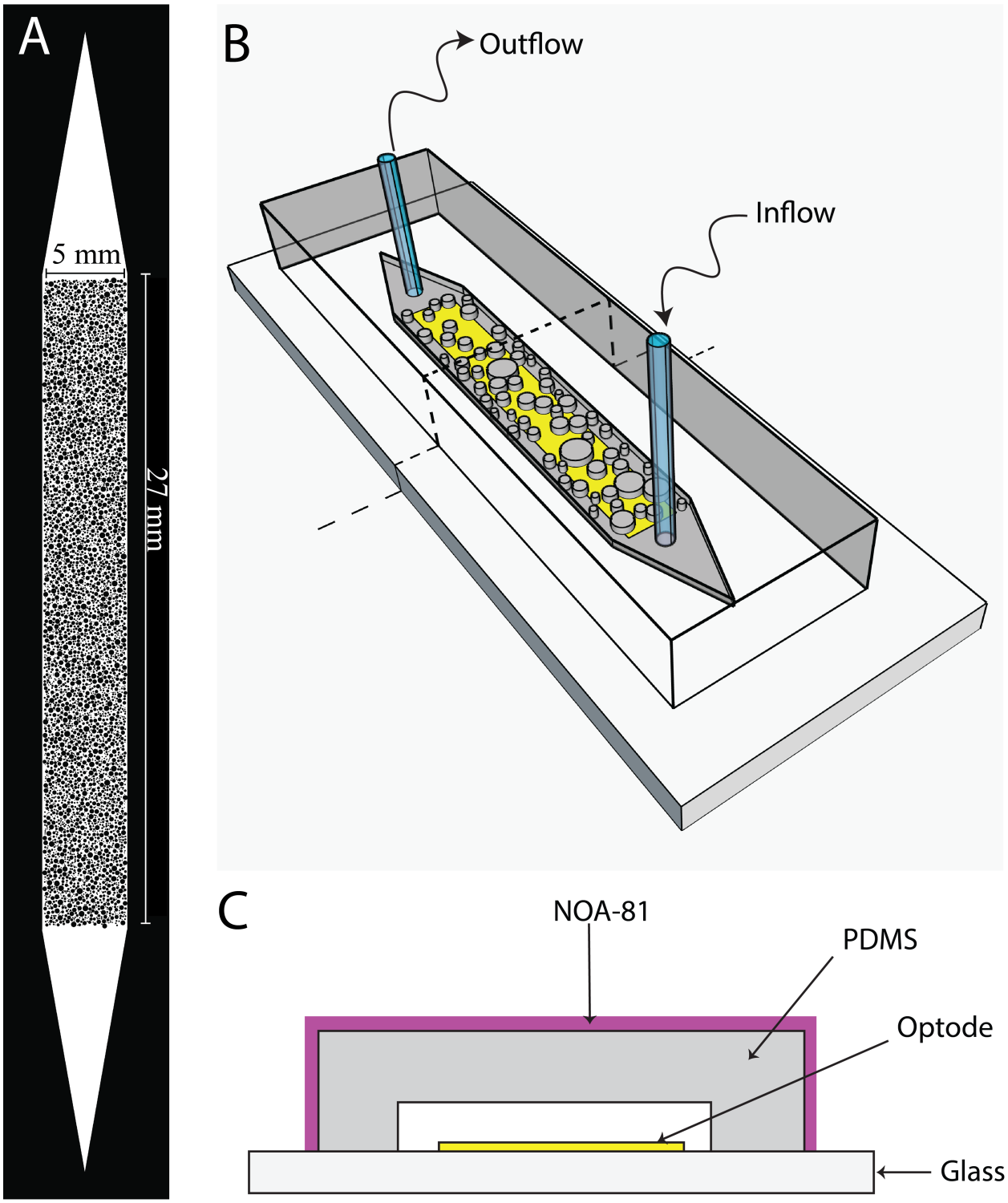

Figure 1: (A) Porous medium geometry used in the experiments. (B) Outline of the microfluidics device composed of glass slide for microscopy, transparent O_2 planar sensor, the PDMS chip engraving the porous medium geometry. Two tubes are connected the pore space of the chip to impose the desired flow conditions. (C) Cross-section of the microfluidics device (dashed black line in panel B) highlighting the layered structure of the chip.

luminescent signals of the two dyes composing the optodes using custom-made filter cubes (Semrock single bandpass (500 ± 20 nm) and Semrock single-band pass filter (662±11) nm). The Lumencor SPECTRA-X LED Light Engine, irradiating at 450 nm, was used for dye excitation.

Large images were obtained by stitching together 40 gray-scale pictures (16-bit) into a single image of $24,522 \times 2,814$ pixels (equivalent to 26.97 mm by 3.09 mm), capturing the entire planar sensor surface.

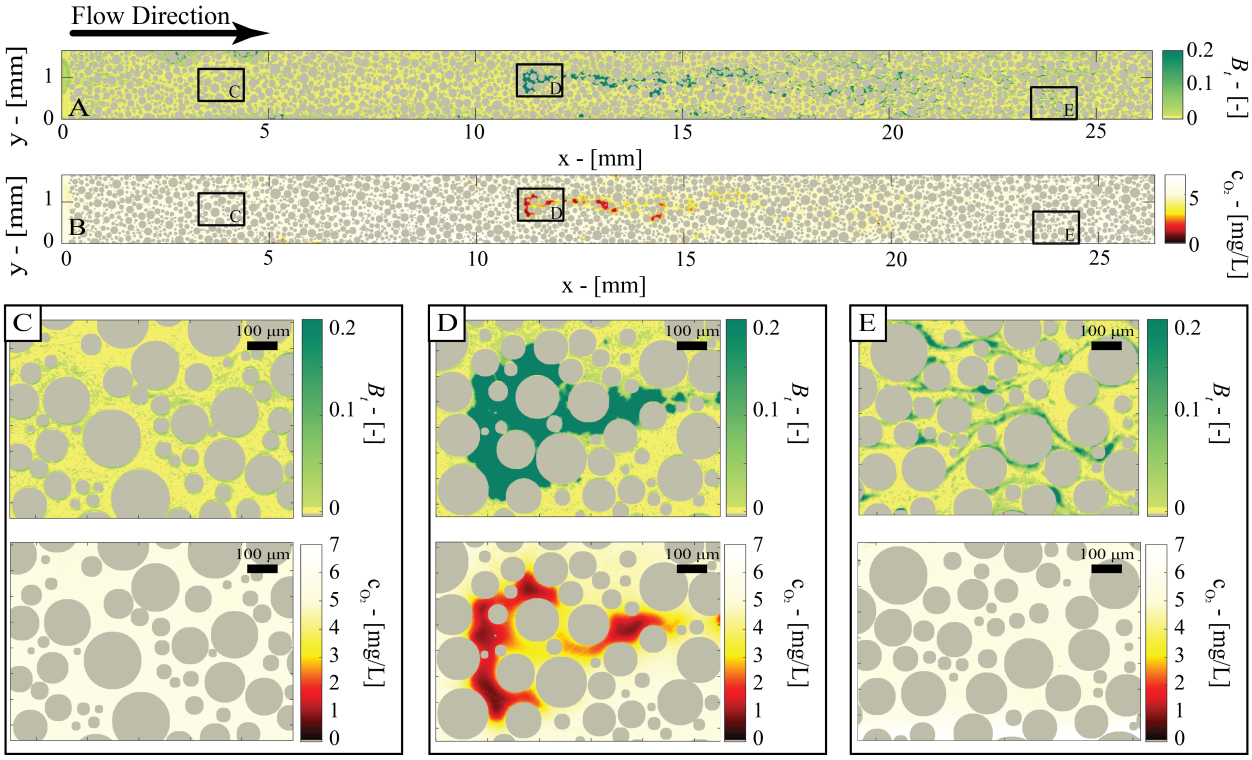

Figure 2: Spatial maps of the biomass B_t (A) and O_2 concentration c_{O_2} (B) at 47 t_{PV} for limited O_2 supply (NOA-81 coated chip). (C-E) Zoom-ins of portions of O_2 map and biomass distribution presented in panel A and B delimited by solid black lines. Grey disks represent solid grains.

Image processing and bulk quantities.

The images collected during each experiment were post-processed to describe porous geometry, spatial and temporal maps of biomass and O_2 concentration at the pore scale. The porous geometry was obtained from an image taken before the inoculation with the adjusted

phase-contrast configuration and stored as a binary matrix M with zero value assigned to solid grains, one otherwise (see further details in the SI, section S3). Hereafter, the solid grains are displayed in all the spatial maps as gray disks which are systematically removed from images analyses (e.g., Figure 2).

The maps of biomass distribution over time, B_t, were obtained by identifying differences in the light intensity between the adjusted phase-contrast image at time t against the image at $t = 0$. Even though we did not directly correlate the B_t maps to well-established metrics for biomass density (e.g., carbon density or Optical Density), we used the dynamics of B_t as a proxy for biomass growth. The concentration c_{O_2} of dissolved oxygen was obtained by dividing the O_2-sensitive optode signal by the reference one and converting this ratio into O_2 concentration values via a proper calibration procedure (described in the SI, section S2). The average biomass growth and O_2 concentration in the system are defined as $E[B_t]$ and $E[O_2]$, computed as:

$$E[B_t](t) = \frac{\sum_i B_t(i,t)}{\sum_i M(i)} \quad \text{and} \quad E[c_{O_2}](t) = \frac{\sum_i c_{O_2}(i,t)}{\sum_i M(i)} \tag{1}$$

where i is the image pixel counter and M the aforesaid geometry binary matrix, which is time-independent.

Results and Discussion

Bulk measurements do not capture micro-scale biogeochemical heterogeneity. The temporal behavior of the bulk O_2 concentration in our porous systems, $E[O_2]$ (Figure 3A), depends on the extent and distribution of O_2 supply in microfluidic device. On the one hand, when O_2 was allowed to freely diffuse thought the PDMS walls of the uncoated chips (used as control), the bulk dissolved O_2 concentration was constant over time and in equilibrium with the atmosphere (about 8.2 mg/L). On the other hand, when the oxygen

supply was limited to the inlet flow (by chip coating with transparent NOA-81 glue), the bulk O_2 concentration decreased to 5.5-6.5 mg/L. The temporal behavior of $E[O_2]$ is mirrored by the quantity Tr_{O_2} (solid black line in Figure 3A), which represents the chosen O_2 concentration threshold for the identification of the anoxic micro-environments and it will be deeply discussed in the following section.

The O_2 supplied by the constant fluid injection was sufficiently high in both scenarios to not limit the overall biomass growth, quantified by $E[B_t]$ (Figure 3B). The latter exhibits the same logistic trend[43] for the coated and uncoated scenarios. The exponential growth lasts until 50 pore volumes have been injected ($1t_{PV} = 33\ min$) and it was followed by a stationary phase (for $t > 50\ t_{PV}$) possibly indicating that the system reached its carrying capacity.

Bulk O_2 (Figure 3A) decreased during exponential growth when bacterial O_2 consumption was high and increased again during stationary phase when the consumption rate slowed down. The overall impact of bacterial activity on bulk O_2 was mild and the system can still be considered highly oxygenated for the entire experiment duration.[4] Then, both scenarios (coated and uncoated chips) can be considered macroscopically well-oxygenated.

Though bulk O_2 concentrations in our coated and uncoated systems remained relatively high and sustained similar biomass growth, micro-scale O_2 distribution differed remarkably (Figure 2A for the coated system and Figures S.10 and S.11 for the uncoated one in SI, section S8). In the gas permeable (uncoated) system, O_2 concentrations were homogeneous while in the impermeable (coated) system anoxic micro-environments formed throughout the porous landscape (Figure 2A). This result provides evidence that low-oxygen spots may form and persist in well-oxygenated porous systems such as groundwater, saturated soils during intense rain events, and river sediments. Furthermore, the anoxic zones persist for several hours during the stationary phase and are still detectable after 55 t_{PV} (i.e., after 5 hours

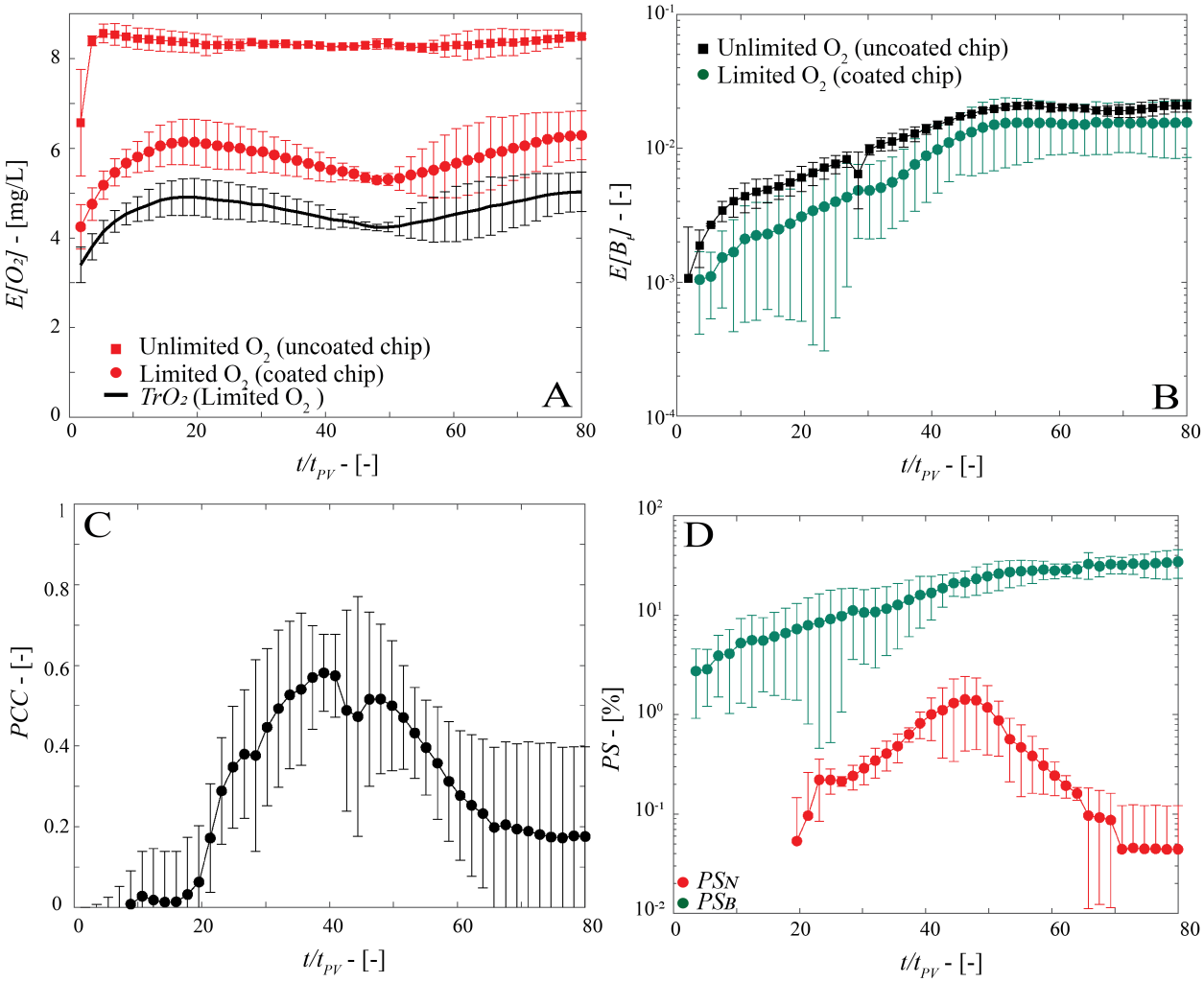

Figure 3: Temporal behavior of bulk quantities $E[O_2]$ (A) and $E[B_t]$ (B), computed according to Eq. 1, for coated (circles) and uncoated (squares) systems. The solid black line in panel A indicates the thresholds (TrO_2) used to identify the anoxic micro-environments in the limited O_2 supply experiment (NOA-81 coated chip). (C) Temporal behavior of the adjusted Pearson Correlation Coefficient (PCC, mathematical definition is detailed in SI, section S4) for the coated system. (D) Temporal behavior of the pore space percentage occupied by anoxic micro-environments (PS_N) and by biomass (PS_B) for the coated system. Symbols indicate averaged values and the errorbars denote the associated standard deviation of replicates.

from the beginning of the stationary phase; see SI, section S6). This evidence suggests that bacterial colonies, even though not expanding their size, are still up-taking O_2. Otherwise, such small-scale gradients would have been smoothed out by diffusion within a time scale of a few seconds. Then, bulk monitoring does not capture the persistence of anoxic micro-environments and overlooks heterogeneity at the scale of interest for bacteria.

Anoxic micro-environments are correlated to bacterial colony aerobic respiration in space and time.

The spatial correlation between O_2-depleted zones and biomass density is quantified through an adjusted Pearson Correlation Coefficient (PCC in Figure 3C, details on the mathematical definition in the SI, section S4). A high positive spatial correlation is observed from $20t_{PV}$ (with a maximum of PCC$\sim$ 0.6), which includes the both the exponential and the following stationary phases of the system. This suggests that the spatial organization of bacterial colonies controls the formation of localized O_2-depleted zones, or anoxic micro-environments.

Identifying anoxic micro-environments is often performed by fixing an absolute O_2 concentration threshold that still does not have an established universal value.[1] Alternatively, one can define anoxic micro-environments as those zones where facultative anaerobic bacteria use electron acceptors other than O_2. Even though conceptually plain, the identification of anoxic micro-environments remains not trivial. Indeed, each facultative strain realistically switches its metabolism at different O_2 concentrations.[27,44] In this framework, the O_2 concentration threshold for anoxic micro-environments identification is inevitably strain- and environment-specific. In this work, we do not investigate any metabolism switch and choose the threshold Tr_{O_2} from the statistical analysis of the O_2 concentration maps (details in the SI, section S5). Base on this analysis, we defined anoxic micro-environments as the portions of the pore space where O_2 concentration (c_{O_2}) is at least 20% lower than the bulk $E[O_2]$ measurements. As a consequence of its definition, the threshold Tr_{O_2} ($\sim 0.8\ E[O_2]$ shown

in Figure 3A) is not a constant absolute value but rather system-specific and time-dependent.

We used TrO_2 to compute the percentage of pore space occupied by anoxic micro-environments PS_N (i.e., the pore space fraction where $c_{O_2} < TrO_2$, see SI, section S3) at each time t (Figure 3D). In addition to the correlation with biomass distribution, anoxic micro-environments formation exhibits a temporal dependence on biomass growth rate. For $t < 50t_{PV}$, anoxic micro-environments progressively increase in volume mirroring biomass exponential growth (Figure 3B). During the stationary phase ($t > 50t_{PV}$), O_2 distribution becomes progressively more homogeneous and the anoxic micro-environments disappear (see SI, section S5, for spatial maps at different times) reflecting the slowdown of bacterial O_2 consumption. The maximum volume of anoxic micro-environments was attained at $46t_{PV}$ accounting for 1 - 2% of the pore space, which is consistent with previous estimates of microbial hotspot occurrence.[9] This implies that the proportion of space occupied by anoxic micro-environments remains always considerably smaller than the one occupied by biomass at all times as shown by PS_B (Figure 3C) that is defined as the percentage of pore space where $B_t > 0$ (see SI for details, section S3).

Our findings indicate that biomass growth is a necessary condition and a key controlling factor for anoxic micro-environments formation but, alone, it does not explain the occurrence of micro-environments (see e.g., Figures 2C and E).

Round shape of colonies favors the anoxic micro-environments formation.
We observe that colony morphology significantly deviates from rounded shapes in our flowing porous system (Figure 2A), which confirms previous findings.[22] Colonies that grow radially are often associated with remarkable localized O_2 depletion (Figure 2D). In contrast, elongated structures along flow direction do not affect local O_2 content (Figure 2E). This work does not focus on processes governing colony morphology, which are investigated elsewhere.[23]

Instead, we draw the attention to the role of colony morphology in controlling anoxic micro-environments formation.

To characterize colony morphology, each cluster of connected pixels colonized by biomass was identified in biomass spatial maps (B_t) and labeled as a distinct bacterial colony. All the colonies were described in terms of planar area A, perimeter P, and the equivalent radius (defined as $R_{EQ} = \sqrt{A/\pi}$). The latter is representative of the characteristic length scale of a round colony. In addition to these metrics, we introduce a colony characteristic length scale, alternative to R_{EQ}, defined as $\lambda = 2A/P$ which discriminates between colonies with similar areas but different shapes. This can also be interpreted as the volume-to-surface ratio of 3D colonies adapted to our 2D images. If a colony is rounded, λ approaches R_{EQ} whereas for elongated colonies λ attains values smaller than R_{EQ}.

We expect that the colony area (or volume in 3D systems) is a key factor controlling oxygen uptake: larger areas imply the presence of more bacteria and, likely, faster nutrient an O_2 consumption. However, comparing local O_2 concentration within each colony (labeled *Colony* O_2, normalized to the threshold TrO_2) to colony area A in Figure 4A, we found that colony area A cannot fully explain the formation of anoxic micro-environments which are observed in colonies of any size. Colony oxygen value appears instead to be controlled by the combination of colony planar area and the characteristic length λ (or colony volume-to-surface ration in 3D systems), related to colony morphology (Figure 4B). Fixed the area, colonies with low O_2 concentration are characterized by higher λ which corresponds to almost rounded shape (or spherical shape in 3D).

Morphology impacts O_2 diffusion into bacterial colonies.

The importance of colony morphology in many ecological processes, such as antibiotic resistance and genetic diversity, has been widely well-recognized.[45,46] This has encouraged an important research effort to understand key factors controlling the dynamics of colony ex-

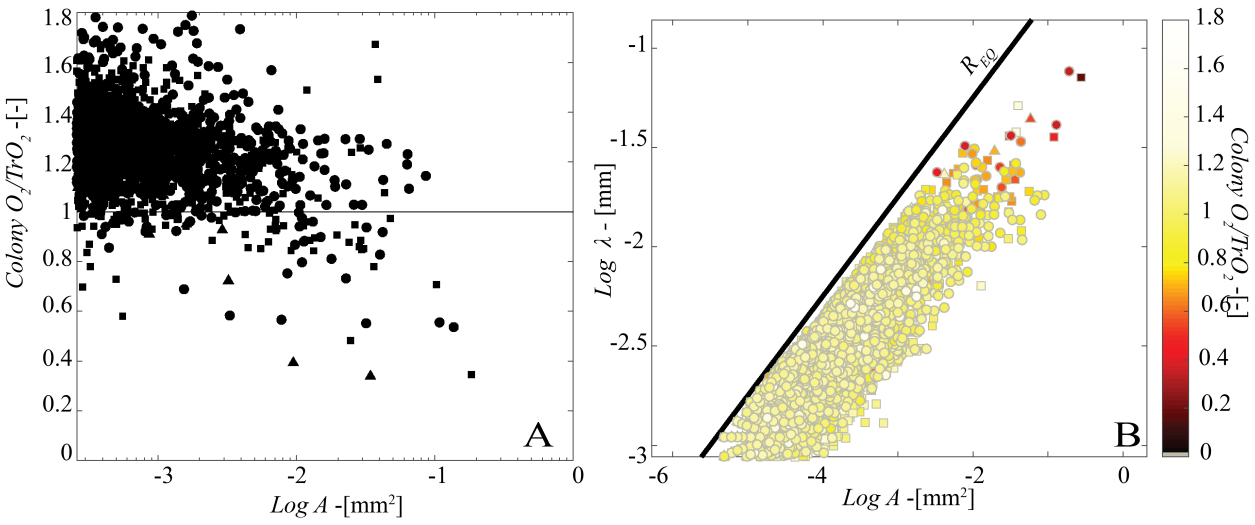

Figure 4: (A) Local O_2 concentration observed in each colony ($Colony\ O_2$) normalized to the threshold (Tr_O2) as a function of the colony area (A) at 47 t_{PV} for the O_2 impermeable system. (B) Characteristic colony length scale λ as a function of the colony area for O_2 supply limited to inlet flow at $47t_{PV}$. Here, marker fill color indicates the local O_2 concentration observed in each colony ($Colony\ O_2$) normalized to the threshold (Tr_O2). In both panels, circles, squares and triangles refer different experiment replica.

pansion and the consequent morphology. Among these, the spatial and temporal distribution of nutrients is pivotal: the combined effect of limited nutrient availability in the bulk system, the diffusion process and bacterial nutrient uptake guide the colony morpho-dynamics.[24,46] As a feedback, the growing pattern modifies physical and chemical properties, such as O_2 concentrations, in the colony core and its surrounding environment. This previous research, involving numerical simulations and laboratory experiments, has nonetheless focused on stagnant systems.[24,45,47] Here, we propose that the role played by colony morphology remains crucial also under flow conditions in complex porous geometries. Our data set, with the simultaneous observation of O_2 and biomass maps, allows to directly assess the impact of morphology on anoxic micro-environments formation. This has been done by investigating the two mechanisms regulating O_2 dynamics at the pore scale: the O_2 uptake associated with aerobic metabolism and the diffusion process transporting O_2 from the pore water to the colony core.

To this end, we simplified the colony morphology into an elongated hemicylinder (for filamentous colonies, Figure 5A) or a hemisphere (for rounded ones, Figure 5B). These colonies lay on sensor surface and the outer surfaces are in contact with flowing O_2-rich pore water. The characteristic length λ represents the shortest distance between the colony core and the surrounding pore water which corresponds to the diffusive path for nutrients and oxygen within the colony.

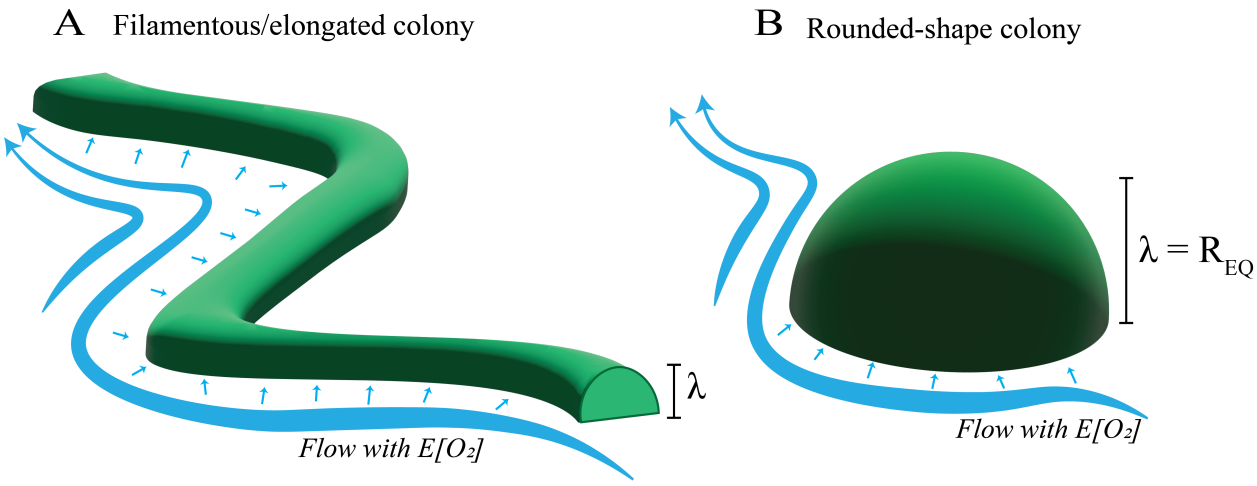

Figure 5: Schematic representation of two paradigmatic colony morphology observed during the experiment: filamentous colony simplified as a hemicylinder (A) and rounded shape simplified as a hemisphere (B).

It is well-established that bacterial growth takes place preferentially at the outer surface of each colony in contact with the pore water that is nutrients and O_2-rich.[24] Even though the thickness of the active layer varies with the bacterial specific growth rate and the bulk nutrient concentration,[24] we can assume that O_2 uptake by a colony is first and foremost dependent on its surface area, approximated by planar area A in our 2D images. According to the first Fick's law, the O_2 diffusion rate is enhanced by a shorter diffusive path (as this generates steeper gradients). Moreover, the overall O_2 diffusive mass flux is favored by a

higher colony outer surface which is proportional to the mass transfer among pore water and colony. Both colony surface and diffusive path length depends on colony morphology (see schematic Figure 5). Given a fixed colony surface, O_2 diffusion into rounded colonies is slower than into elongated due to the smaller volume-to-surface ratio (longer diffusion path λ).

Morphology significantly alters O_2 mass balance in the colony.

We argue that colony shape alters O_2 diffusive flux enough to tip the balance from transport to bacterial O_2 uptake triggering anoxic micro-environments formation. We therefore propose a quantitative relationship between O_2 biomass consumption rate (R_C, [mol O_2/s]) and O_2 diffusion rate (R_T, [mol O_2/s]. This *ad hoc* Damköhler number (typically defined for abiotic reactions[48]) accounts for colony morphology:

$$Da(\lambda) = \frac{R_C}{R_T} = \frac{\mu_B \, Y \, \rho}{D_m \, \nabla c_{O_2}(\lambda) A}. \tag{2}$$

The external surface area of the colony that should appear in R_T according to the first Fick's law is approximated in Eq. 2 by the planar area A observable from biomass maps.

The quantity μ_B [mm^3/s] measures the colony growth rate as volumetric change. Under the assumption that colony growth takes place mainly on the outer surface,[26] μ_B is proportional to the colony area increasing rate ($\delta \, A/\delta t$) and the to volume-to-surface ratio of an individual bacterium during exponential phase ($\sim 1 \cdot 10^{-3}$ mm, assuming a cylindrical cell with a basal radius of ~ 0.6 μm). Then, μ_B of each colony is estimated from temporal behavior of colony area observed in biomass maps.

The O_2 concentration gradient between the pore water and colony core, $\nabla c_{O_2}(\lambda)$ [mol O_2/mm^4] is expressed as an explicit function of colony morphology through λ. It scales as the ratio

$E[O_2]/\lambda$, being $E[O_2]$ the O_2 concentration in pore water (assumed equal to the bulk one) and λ the diffusion path length determined by colony morphology (see Figure 5). The three parameters ρ [molC/mm^3] , Y [molO_2/molC], and D_m [mm^2/s] quantify, respectively, the amount of carbon per volumetric unit of biomass, the bacterial O_2 demand and O_2 molecular diffusion coefficient as they appear in the literature ($\rho = 4.6\ 10^{-5}$ molC/mm^3 for *P. putida* strains; $Y = 11$ molO_2/molC; $2 \cdot 10^{-3}$ mm^2/s).[49,50]

Our results suggest that morphology quantitatively impacts O_2 balance inside bacterial colonies since $Da(\lambda)$ spans from 0.4 to 2.5 for colonies of similar areas (Figure 6A). Local O_2 concentrations observed in colonies is well-explained by the conceptual model proposed where *Colony* O_2 decreases, on average, for increasing $Da(\lambda)$, as clearly highlighted by the average data trend (solid red line in Figure 6A). The latter shows a marked decreasing behavior of *Colony* O_2 for increasing $Da(\lambda)$ and falls below the O_2 threshold when $Da(\lambda) > 1$. According to our metric, conditions compatible with anoxic micro-environments formation (i.e., $Da(\lambda) > 1$) are expected in the 1% of the pore space which is consistent with the value of pore space occupied by anoxic micro-environments obtained from spatial map analyses (PS_N, Figure 3D). Our metric $Da(\lambda)$ correctly predicts the observed local O_2 concentration in the 96% of the colonies analyzed (see e.g., Figures 6C-D). A few colonies present morphological features leading to $Da(\lambda) > 1$ but maintain relatively high local oxygen levels ($1 < Colony\ O_2/Tr_{O_2} < 1.2$). This misinterpretation is limited to a minor percentage of colonies (about 0.6%) and their local O_2 concentration was still lower than the bulk one $E[O_2]$.

This is further confirmed by the computed average colony O_2 behavior (solid red line in Figure 6*B*) as a function of $Da(R_{EQ})$: colony O_2 for $Da(R_{EQ}) > 1$ attains similar mean values of colonies characterized by $Da(R_{EQ}) < 1$: in other words, it is much less sensitive to $Da(R_{EQ})$ variations. Neglecting morphology (i.e. considering $Da(R_{EQ})$) leads to over-

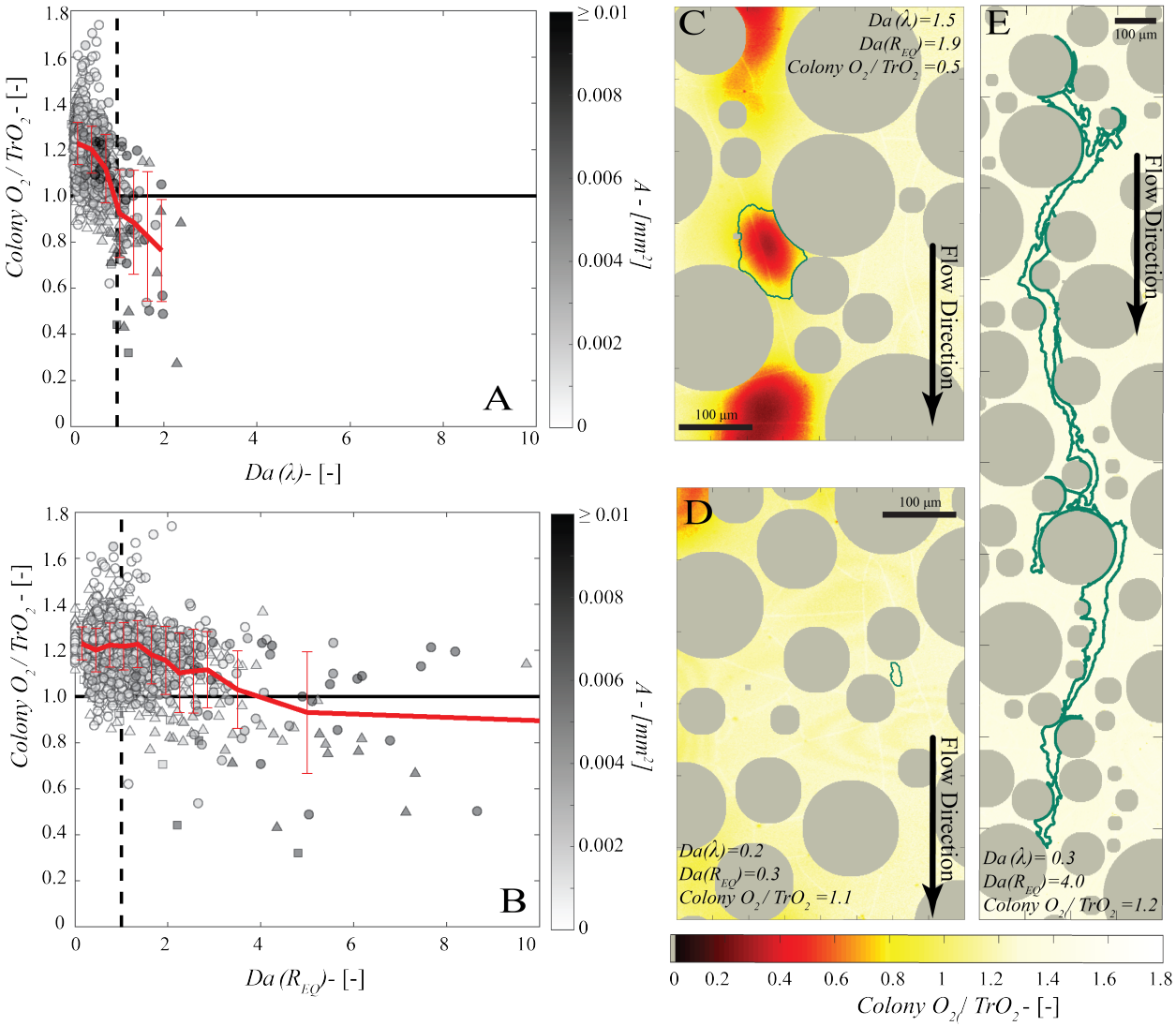

Figure 6: (A) The observed local O_2 concentration within each colony (normalized by the threshold $Colony\ O_2/Tr_{O_2}$) against the computed value of $Da(\lambda)$. Data presented are averaged between 25 and 65 t_{PV} during which micro-environments persist. Time variability is discussed in SI, section S7. The dashed vertical line denotes the $Da = 1$ which distinguishes O_2 diffusion dominated colonies ($Da < 1$) from conditions suitable for anoxic micro-environments formation ($Da > 1$). The horizontal solid lines represents the threshold ($Colony\ O_2/Tr_{O_2}$) used to discriminate between well-oxygenated and anoxic colonies. Marker face colors indicate the colony area A. The solid red line highlights the average trend of data and the associate standard deviation (vertical errorbars) obtaining by bining Da data into sequential intervals and computing the mean and the standard deviation of $Colony\ O_2/Tr_{O_2}$ data within each bin. (B) Same as panel A with Da computed by replacing λ with R_{EQ} in Eq. 2 and indicated as $Da(R_{EQ})$. (C-E) Zooms of the O_2 spatial map (normalized to the O_2 threshold Tr_{O_2}) at $47t_{PV}$ of two rounded colonies of different sizes (C and D) and an elongated colony (E). The colony location is identified by its perimeter (green line). Value of $Da(\lambda)$, $Da(R_{EQ})$ and local oxygen concentration are reported.

estimating the occurrence of anoxic micro-environments to 30% of the colonies. Indeed, $Da(R_{EQ}) > 1$ are associated with extended filamentous colonies (see e.g., Figure 6E) which remain locally well-oxygenated. We finally highlight that the robustness of the $Da(\lambda)$ metric has been tested with different Tr_{O_2} and the crucial role played by morphology is invariant to the O_2 threshold imposed for the anoxic micro-environments identification (see SI, section 5).

Environmental Implications Our results show that the formation and persistence of anoxic micro-environments (up to 2% of the pore space) occur in saturated heterogeneous porous environments despite the continuous injection of well-oxygenated flow. This evidence suggests that excluding the alternative metabolisms of facultative anaerobic bacteria in saturated porous media based on their bulk oxygen content (still commonly done in geochemical modeling of the subsurface environments) would lead to an oversimplification and underestimation of the facultative metabolism contribution to element cycling and contaminant attenuation/mobilization. Our work, using a simplified scenario, provides new insights on the pivotal role of colony morphology on local physical-chemical properties under flow conditions that might help explaining the tiny portion of the porous space occupy by anoxic micro-environments observed in well-oxygenated real subsurface system. Moreover, the proposed metric $Da(\lambda)$, can be adjusted to describe the strain of interest and combined with dedicated models interpreting bacterial colony spatial organization in porous media.[51] This will constitute a preliminary predictive tool to identify bacterial colonies that are prone to become anoxic micro-environments and estimate the portion of anoxic pore space in well-oxygenated porous systems.

Though the proposed metric can be, in principle, applied to colonies in complex 3D systems, its validity is yet to be tested in such scenarios. Our experimental set-up is limited to 2D geometries representing the pore size heterogeneity and not other structural features typical of natural sediments, e.g., variable surface roughness, the composition of the grains, and

nutrient-rich solid aggregates. Moreover, the microbial ecology considered in this study is highly simplified since it accounts for and investigates a laboratory isolate. Still, the strain used in this work belongs to the naturally widespread gender of Pseudomonas. Thus, its behavior might be similar to other strains found in nature, especially if we consider that, according to recent studies,[46] colony morphology might be less sensitive to bacterial strain than expected. A large number of factors that might play a key role in anoxic micro-environments formation are yet to be explored, including the use of a more complex bacterial consortium, different porous geometries, and initial/boundary conditions (e.g., pore space saturation level, alternation of stagnant and flow periods, different nutrient spatial and temporal concentration distribution).

Moreover, longer experiment runs are needed to investigate the possible intermittent behavior of anoxic micro-environments[9] and the effect of flow shear stress on the stability of the bacterial clusters. Our innovative methodology, merging easily manipulable microfluidic devices with transparent planar sensors, is flexible and allows individual exploration of all these factors in a fully-controlled laboratory environment. Finally, we highlight that our methodology may find valuable applications to all those disciplines interested in O_2 heterogeneity such as bioremediation engineering[12] and biomedical/veterinary studies.[52]

Acknowledgements

Pietro de Anna acknowledges the support of Swiss National Science Foundation, Project No. 200021_172587, *Flows in confined micro-structures: Coupling physical heterogeneity and biochemical processes.* Giulia Ceriotti acknowledges support from the *Swiss FCS Postdoctoral Excellence Fellowship.*

Supporting Information Available

Details on O_2 planar sensors function and calibration; description of the procedures employed to process images collected during the microfluidics experiments; description of the adjusted Pearson Correlation Coefficient used in this study to characterize spatial correlation of biomass and O_2 depletion; high-resolution images of biomass and oxygen maps at different times for all replicates of the coated system; discussion about temporal variability of Damköhler number; high-resolution images of biomass and oxygen maps at different times for all replicates of the uncoated system and analyses of results associated with this control scenario.

References

(1) Berg, J. S.; Ahmerkamp, S.; Pjevac, P.; Hausmann, B.; Milucka, J.; Kuypers, M. M. How low can they go? Aerobic respiration by microorganisms under apparent anoxia. *FEMS Microbiology Reviews* **2022**,

(2) Or, D.; Smets, B. F.; Wraith, J.; Dechesne, A.; Friedman, S. Physical constraints affecting bacterial habitats and activity in unsaturated porous media–a review. *Advances in Water Resources* **2007**, *30*, 1505–1527.

(3) Pedersen, L. L.; Smets, B. F.; Dechesne, A. Measuring biogeochemical heterogeneity at the micro scale in soils and sediments. *Soil Biology and Biochemistry* **2015**, *90*, 122–138.

(4) Keiluweit, M.; Gee, K.; Denney, A.; Fendorf, S. Anoxic microsites in upland soils dominantly controlled by clay content. *Soil Biology and Biochemistry* **2018**, *118*, 42–50.

(5) Haberer, C. M.; Rolle, M.; Liu, S.; Cirpka, O. A.; Grathwohl, P. A high-resolution non-invasive approach to quantify oxygen transport across the capillary fringe and within the underlying groundwater. *Journal of contaminant hydrology* **2011**, *122*, 26–39.

(6) Parker, S. R.; Darvis, M. N.; Poulson, S. R.; Gammons, C. H.; Stanford, J. A. Dissolved oxygen and dissolved inorganic carbon stable isotope composition and concentration fluxes across several shallow floodplain aquifers and in a diffusion experiment. *Biogeochemistry* **2014**, *117*, 539–552.

(7) Herath, I.; Vithanage, M.; Bundschuh, J.; Maity, J. P.; Bhattacharya, P. Natural arsenic in global groundwaters: distribution and geochemical triggers for mobilization. *Current Pollution Reports* **2016**, *2*, 68–89.

(8) Boschetti, T.; Toscani, L. Springs and streams of the Taro–Ceno Valleys (Northern Apennine, Italy): reaction path modeling of waters interacting with serpentinized ultramafic rocks. *Chemical Geology* **2008**, *257*, 76–91.

(9) Kravchenko, A.; Toosi, E.; Guber, A.; Ostrom, N.; Yu, J.; Azeem, K.; Rivers, M.; Robertson, G. Hotspots of soil N2O emission enhanced through water absorption by plant residue. *Nature Geoscience* **2017**, *10*, 496–500.

(10) Kuzyakov, Y.; Blagodatskaya, E. Microbial hotspots and hot moments in soil: concept & review. *Soil Biology and Biochemistry* **2015**, *83*, 184–199.

(11) Rubol, S.; Dutta, T.; Rocchini, D. 2D visualization captures the local heterogeneity of oxidative metabolism across soils from diverse land-use. *Science of the Total Environment* **2016**, *572*, 713–723.

(12) Schramm, A.; Santegoeds, C. M.; Nielsen, H. K.; Ploug, H.; Wagner, M.; Pribyl, M.; Wanner, J.; Amann, R.; de Beer, D. On the occurrence of anoxic microniches, denitrification, and sulfate reduction in aerated activated sludge. *Applied and Environmental Microbiology* **1999**, *65*, 4189–4196.

(13) Keiluweit, M.; Wanzek, T.; Kleber, M.; Nico, P.; Fendorf, S. Anaerobic microsites have an unaccounted role in soil carbon stabilization. *Nature communications* **2017**, *8*, 1–10.

(14) Herrero, J.; Puigserver, D.; Nijenhuis, I.; Kuntze, K.; Carmona, J. M. Key factors controlling microbial distribution on a DNAPL source area. *Environmental Science and Pollution Research* **2022**, *29*, 1508–1520.

(15) Visser, A.-N.; Lehmann, M. F.; Rügner, H.; D'Affonseca, F. M.; Grathwohl, P.; Blackwell, N.; Kappler, A.; Osenbrück, K. Fate of nitrate during groundwater recharge in a fractured karst aquifer in Southwest Germany. *Hydrogeology Journal* **2021**, *29*, 1153–1171.

(16) Baveye, P. C.; Otten, W.; Kravchenko, A.; Balseiro-Romero, M.; Beckers, É.; Chalhoub, M.; Darnault, C.; Eickhorst, T.; Garnier, P.; Hapca, S., et al. Emergent properties of microbial activity in heterogeneous soil microenvironments: different research approaches are slowly converging, yet major challenges remain. *Frontiers in Microbiology* **2018**, *9*, 1929.

(17) Smriga, S.; Ciccarese, D.; Babbin, A. R. Denitrifying bacteria respond to and shape microscale gradients within particulate matrices. *Communications Biology* **2021**, *4*, 1–9.

(18) de Anna, P.; Pahlavan, A. A.; Yawata, Y.; Stocker, R.; Juanes, R. Chemotaxis under flow disorder shapes microbial dispersion in porous media. *Nature Physics* **2021**, *17*, 68–73.

(19) Zhang, C.; Kang, Q.; Wang, X.; Zilles, J. L.; Muller, R. H.; Werth, C. J. Effects of pore-scale heterogeneity and transverse mixing on bacterial growth in porous media. *Environmental science & technology* **2010**, *44*, 3085–3092.

(20) Hamada, M.; Cueto-Felguroso, L.; de Anna, P. Diffusion limited mixing in confined media. *Physical Review Fluids* **2020**, *5*.

(21) Franklin, S.; Vasilas, B.; Jin, Y. More than meets the dye: Evaluating preferential flow paths as microbial hotspots. *Vadose Zone Journal* **2019**, *18*, 1–8.

(22) Hommel, J.; Coltman, E.; Class, H. Porosity–permeability relations for evolving pore space: a review with a focus on (bio-) geochemically altered porous media. *Transport in Porous Media* **2018**, *124*, 589–629.

(23) Carrel, M.; Morales, V. L.; Beltran, M. A.; Derlon, N.; Kaufmann, R.; Morgenroth, E.; Holzner, M. Biofilms in 3D porous media: Delineating the influence of the pore network geometry, flow and mass transfer on biofilm development. *Water research* **2018**, *134*, 280–291.

(24) Young, E.; Melaugh, G.; Allen, R. J. Pinning transition in biofilm structure driven by active layer dynamics. *bioRxiv* **2022**,

(25) Tronnolone, H.; Tam, A.; Szenczi, Z.; Green, J.; Balasuriya, S.; Tek, E. L.; Gardner, J. M.; Sundstrom, J. F.; Jiranek, V.; Oliver, S. G., et al. Diffusion-limited growth of microbial colonies. *Scientific Reports* **2018**, *8*, 1–11.

(26) Vulin, C.; Di Meglio, J.-M.; Lindner, A. B.; Daerr, A.; Murray, A.; Hersen, P. Growing yeast into cylindrical colonies. *Biophysical Journal* **2014**, *106*, 2214–2221.

(27) Marchant, H. K.; Ahmerkamp, S.; Lavik, G.; Tegetmeyer, H. E.; Graf, J.; Klatt, J. M.; Holtappels, M.; Walpersdorf, E.; Kuypers, M. M. Denitrifying community in coastal sediments performs aerobic and anaerobic respiration simultaneously. *The ISME journal* **2017**, *11*, 1799–1812.

(28) Pedraz, L.; Blanco-Cabra, N.; Torrents, E. Gradual adaptation of facultative anaerobic pathogens to microaerobic and anaerobic conditions. *The FASEB Journal* **2020**, *34*, 2912–2928.

(29) Groffman, P. M.; Butterbach-Bahl, K.; Fulweiler, R. W.; Gold, A. J.; Morse, J. L.; Stander, E. K.; Tague, C.; Tonitto, C.; Vidon, P. Challenges to incorporating spatially and temporally explicit phenomena (hotspots and hot moments) in denitrification models. *Biogeochemistry* **2009**, *93*, 49–77.

(30) Raven, M.; Keil, R.; Webb, S. Microbial sulfate reduction and organic sulfur formation in sinking marine particles. *Science* **2021**, *371*, 178–181.

(31) Ye, W.; Zhang, G.; Zheng, W.; Zhang, H.; Wu, Y. Methane distributions and sea-to-air fluxes in the Pearl River Estuary and the northern South China sea. *Deep Sea Research Part II: Topical Studies in Oceanography* **2019**, *167*, 34–45.

(32) Bižić, M.; Grossart, H.-P.; Ionescu, D. Methane Paradox. *eLS* 1–11.

(33) Cook, P. L. M.; Kessler, A. J.; Eyre, B. D. Does denitrification occur within porous carbonate sand grains? *Biogeosciences* **2017**, *14*, 4061–4069.

(34) Lehto, N. J.; Larsen, M.; Zhang, H.; Glud, R. N.; Davison, W. A mesocosm study of oxygen and trace metal dynamics in sediment microniches of reactive organic material. *Scientific reports* **2017**, *7*, 1–12.

(35) Widerlund, A.; Davison, W. Size and density distribution of sulfide-producing microniches in lake sediments. *Environmental science & technology* **2007**, *41*, 8044–8049.

(36) Borisov, S. M.; Seifner, R.; Klimant, I. A novel planar optical sensor for simultaneous monitoring of oxygen, carbon dioxide, pH and temperature. *Analytical and bioanalytical chemistry* **2011**, *400*, 2463–2474.

(37) Sun, S.; Ungerböck, B.; Mayr, T. Imaging of oxygen in microreactors and microfluidic systems. *Methods and applications in fluorescence* **2015**, *3*, 034002.

(38) Aleklett, K.; Kiers, E. T.; Ohlsson, P.; Shimizu, T. S.; Caldas, V. E.; Hammer, E. C. Build your own soil: exploring microfluidics to create microbial habitat structures. *The ISME journal* **2018**, *12*, 312–319.

(39) de Anna, P.; Quaife, B.; Biros, G.; Juanes, R. Prediction of the low-velocity distribution from the pore structure in simple porous media. *Physical Review Fluids* **2017**, *2*, 124103.

(40) Scheidweiler, D.; Miele, F.; Peter, H.; Battin, T. J.; de Anna, P. Trait-specific dispersal of bacteria in heterogeneous porous environments: from pore to porous medium scale. *Journal of The Royal Society Interface* **2020**, *17*, 20200046.

(41) Ceriotti, G.; Russian, A.; Bolster, D.; Porta, G. A double-continuum transport model for segregated porous media: Derivation and sensitivity analysis-driven calibration. *Advances in Water Resources* **2019**, *128*, 206–217.

(42) Alhashmi, Z.; Blunt, M.; Bijeljic, B. The impact of pore structure heterogeneity, transport, and reaction conditions on fluid–fluid reaction rate studied on images of pore space. *Transport in Porous Media* **2016**, *115*, 215–237.

(43) Madigan, M. T.; Martinko, J. M.; Dunlap, P. V.; Clark, D. P. Brock biology of microorganisms 12th edn. *Int. Microbiol* **2008**, *11*, 65–73.

(44) Angel, R.; Matthies, D.; Conrad, R. Activation of methanogenesis in arid biological soil crusts despite the presence of oxygen. *PloS one* **2011**, *6*, e20453.

(45) Melaugh, G.; Hutchison, J.; Kragh, K. N.; Irie, Y.; Roberts, A.; Bjarnsholt, T.; Diggle, S. P.; Gordon, V. D.; Allen, R. J. Shaping the growth behaviour of biofilms initiated from bacterial aggregates. *PloS one* **2016**, *11*, e0149683.

(46) Martínez-Calvo, A.; Bhattacharjee, T.; Bay, R. K.; Luu, H. N.; Hancock, A. M.; Wingreen, N. S.; Datta, S. S. Roughening instability of growing 3D bacterial colonies. *bioRxiv* **2022**,

(47) Farrell, F.; Hallatschek, O.; Marenduzzo, D.; Waclaw, B. Mechanically driven growth of quasi-two-dimensional microbial colonies. *Physical review letters* **2013**, *111*, 168101.

(48) de Anna, P.; Jimenez-Martinez, J.; Tabuteau, H.; Turuban, R.; Le Borgne, T.; Derrien, M.; Meheust, Y. Mixing and reaction kinetics in porous media: An experimental pore scale quantification. *Environmental science & technology* **2014**, *48*, 508–516.

(49) Fagerbakke, K. M.; Heldal, M.; Norland, S. Content of carbon, nitrogen, oxygen, sulfur and phosphorus in native aquatic and cultured bacteria. *Aquatic Microbial Ecology* **1996**, *10*, 15–27.

(50) Zakem, E.; Follows, M. A theoretical basis for a nanomolar critical oxygen concentration. *Limnology and Oceanography* **2017**, *62*, 795–805.

(51) Tang, Y.; Valocchi, A. J.; Werth, C. J.; Liu, H. An improved pore-scale biofilm model and comparison with a microfluidic flow cell experiment. *Water Resources Research* **2013**, *49*, 8370–8382.

(52) Jensen, P. Ø.; Kolpen, M.; Kragh, K. N.; Kühl, M. Microenvironmental characteristics and physiology of biofilms in chronic infections of CF patients are strongly affected by the host immune response. *Apmis* **2017**, *125*, 276–288.

Supporting Information of "Morphology and size of bacterial colonies control anoxic microenvironment formation in porous media"

Giulia Ceriotti,*,† Sergey M. Borisov,‡ Jasmine Berg,† and Pietro de Anna*,¶

†*Institute of Earth Surface Dynamics, University of Lausanne, Switzerland*

‡*Institute of Analytical Chemistry and Food Chemistry, Graz University of Technology, Austria*

¶*Institute of Earth Sciences, University of Lausanne, Switzerland*

E-mail: giulia.ceriotti@unil.ch; pietro.deanna@unil.ch

S1: Preparation of the planar sensor

An amount of 4 mg of a lipophilic coumarin dye (Bu3Coum)[1]1, 2 mg of platinum(II) meso-pentafluorophenyl porphyrin (Frontier Scientific) and 400 mg of polystyrene (MW 250,000 Da, Acros Organics) were dissolved in 1.6 g of anisole. The obtained solution was screen-printed onto a glass slide with a custom made mask ordered from Welle Oberkirch GmbH (Oberkirch-Zusenhofen, Germany). The glass slides were modified with chlorotrimethylsilane (Aldrich) prior to use.

S2: Optode functioning and calibration

The optode used in this work is a homogeneous solution of two luminescent dyes in solid matrix polymer (polystyrene). One of the dyes (fluorescent coumarin dye) is not sensitive to

oxygen and it constitutes a reference signal. The emission of the second dye (a phosphorescent Pt(II) porphyrin), instead, is quenched by molecular oxygen. The degree of quenching is proportional to the concentration of molecular oxygen.

Both dyes are excited by the same wave length of 450 nm while emitting their luminescence at two different wavelengths. As such, the overall optode emission signal is a superimposition of two spectra and presents two clearly distinguishable fluorescent peaks. Figure S.1 shows the emission spectrum of the optode for an air-saturated and a anoxic water solution. As we can see, the fluorescent peak located at 500 nm shows a slight variation that is associated to external ambient factors and not to the oxygen availability, while the peak located 660 nm remarkably drops when the anoxic solution is replaced by the air-saturated one.

The O_2 concentration assessment is estimated by computing the ratio I_R between the intensity I_{O2} of the 660 nm peak and the intensity I_{ref} of the 500 nm reference peak. In this way, eventual emission fluctuations associated with factors other than O_2 concentration variation are removed since they would affect in the same way both signals I_{O2} and I_{ref}.

As shown in Figure S2 chip (length 55 mm, width 15 mm and thickness 3.5 mm), modeled by purring polydimethylsiloxane (PDMS; Sylgard 184 Silicone Elastomer Kit, Dow Corning, Midland, MI) with the addition of 10 w/w % of curing agent in a plastic mould, is plasma-bonded on top of a microscope glass slide where an optode has been deposited via screen-printing technique. Two Tygon tubes are connected to the chip allowing injecting a chosen solution in the chip chamber. The entire chip surface has been coated with a layer of NOA-81 glue to prevent oxygen in-fluxing from the external atmosphere. A fiber optic O_2 sensor protected by a sharp syringe needle (TROX430, Pyroscience) is speared into the PDMS layer constituting the wall of the chip chamber such that the measuring point is located in close proximity to the planar optode sensor as outlined in Figure S.3. Before the chip

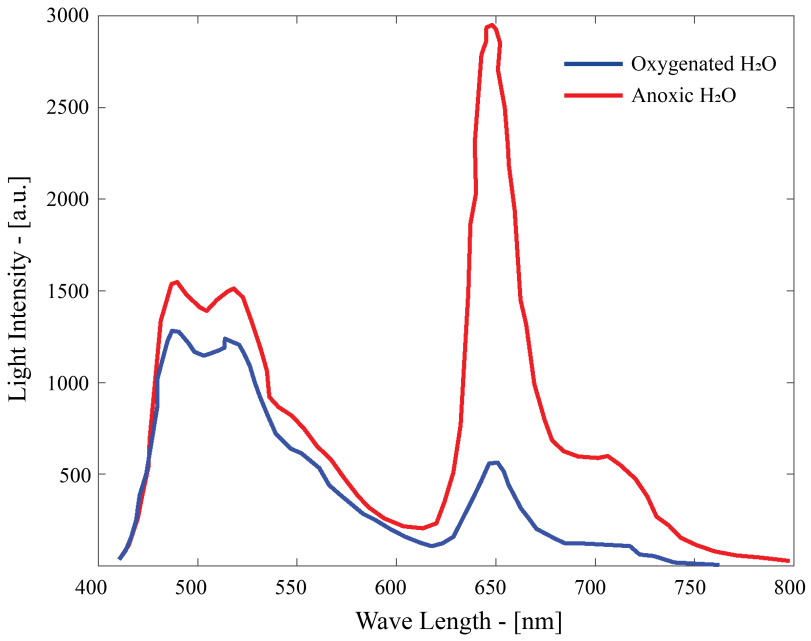

Figure S. 1: Emission spectra of the optodes in an air-saturated solution (blue line) and anoxic solution (red line).

set-up, the fiber optic O_2 sensor is calibrated according to guidelines provided by the supplier.

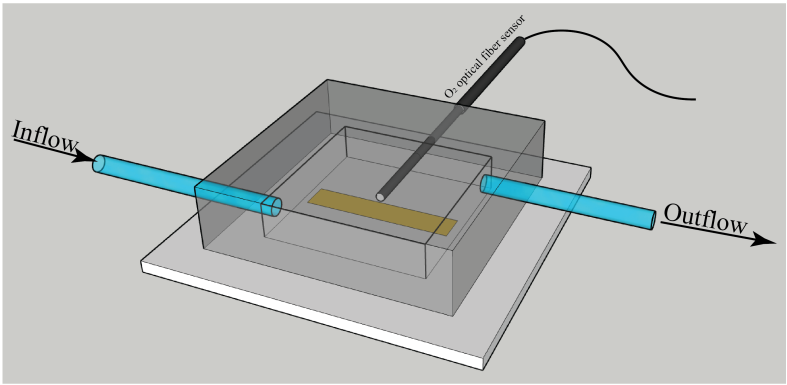

Figure S. 2: Outline of the chip used for optode calibration procedure.

Four water solutions with different dissolved O_2 concentrations are prepared by mixing air-saturated Milli-Q water (S_{high}, obtained by carefully shaking three times a 250 mL Schott bottle filled with 100 mL of Milli- Q water and opening the cap after each shake for few minutes) and a poorly oxygenated Milli-Q water (S_{low}) obtained by dissolving $\simeq$ 8 mg of sodium sulfate in 100 mL of Milli-Q water leading to a solution with O_2 concentration equal

to 0.1 mg/L. The chemical O_2 consumption by sodium sulfate is catalyzed by adding 40 μL of standard Cobalt solution (Merck, $Co(NO_3)_2$ in HNO_3 0.5 mol/l 1000 mg/l Co Certipur®) before mixing. A fully anoxic solution (S_0) is also prepared by adding an excess of sodium sulfate in 100 mL of Milli-Q water.

The chip is placed on a miscrocope stage, 10 mL of each solution, with different dissolved O_2, are separately injected manually into the chip thorough a Benton glass syringe. Two pictures of the optode signal are taken where the optical fiber has been positioned. The first picture captures the reference dye signal by shining the optode with a blue LED (440 ± 20 nm) generated by the Lumencor SPECTRA X Light Engine and filtering the emission signal through a Semrock GFP bandpass emission filter. The second image captures the phosphorescent signal of the O_2 sensitive dye obtained by illuminating the chip with a blue LED (440 ± 20 nm) generated by the same LED and filtering the emission signal through a custom Semrock single-band band pass filter 662 ± 11 nm. Four couples of pictures are taken to test the stability of our optode measurement.

Figure S.3 shows all data collected: the dissolved O_2 concentration measured by the TROX430 are reported against the signal ratio R_I detected for each couple fo pictures. The best fit of these data (solid red line in Figure S.3) is the exponential function

$$c = 29.7\, e^{-2.02\, I_R}. \tag{1}$$

which we found using the MATLAB Curve Fitting App with a confidence level of 95 % on parameter estimated value. The resulting R^2 metric is equal to 0.994.

Overall, the chosen optode sensor presents three major advantages. First, the presence of the sensor on the glass slide does not alter the chip transparency. Second, the employment

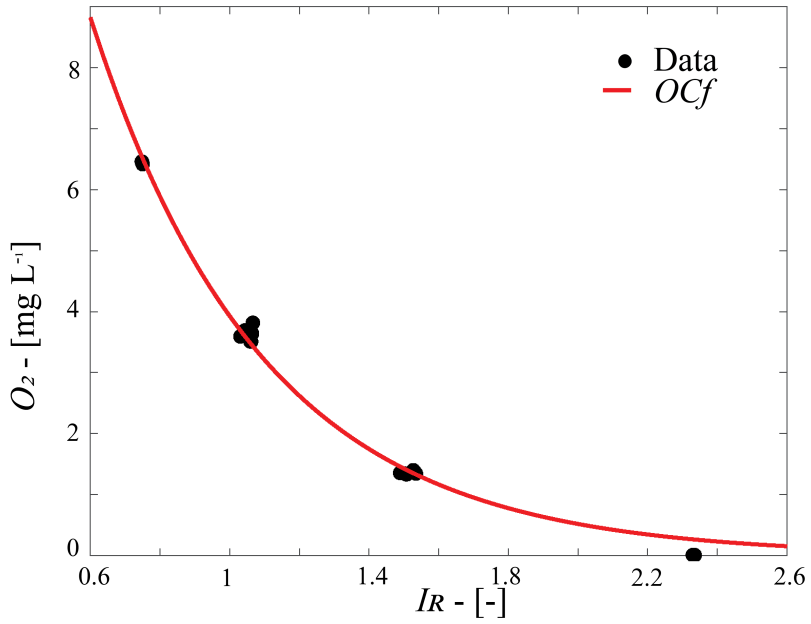

Figure S. 3: Calibration data (black circles) collected during the optode calibration procedure and the fitting curve.

of O_2 sensitive dye in combination with a reference dye provides a robust measurement of dissolved O_2 concentration, which is independent from external environmental conditions and experimental set up (e.g. camera, light source a and objective features). Third, the eventual quenching mechanism does not consume O_2.

S3: Image processing

The mask. We define a binary matrix M, of the same size as the images we acquired to store the information on the porous medium structure. To this end, we use the image acquired with an adjusted phase contrast configuration just before microbial suspension inoculation. We used a large phase ring (Nikon Ph3) compared to the ring (a Ph1) present in the objective, so that the sample gets illuminated almost laterally. This results in a dark background and the perimeter of each grain will appear as a bright circle. First, we set to 0 the value of each pixel below a local threshold value defined by the Matlab function *adaptthresh*: it corresponds to all pixels other than grains' perimeter. Second, exploiting the

Matlab function *imfill*, we assign to all pixels inside a circle a value of 1, obtaining disks of the same size and location as the physical grains. The mask M is then derived as the inverted image of the latter matrix: pixels representing solid grains are associated with the value of 0, and 1 otherwise.

Microbial spatial distribution. Images for biomass distribution were taken with an adjusted phase contrast optical configuration used for mask. In this configuration, bacteria appear as bright spots. To quantify the distribution of bacteria B_t at each acquisition time t, we consider the matrix $I_t(x, y)$ corresponding to the image acquired with the adjusted phase contrast configuration, where x and y represent the longitudinal and transverse spatial directions. First, each element of I is rescaled between 0 (dark pixels) and 1 (white pixel) dividing its value by $2^{16} - 1$ (i.e. the camera pixel depth). Second, we subtract to the rescaled $I_t(x, y)$ the matrix $I_0(x, y)$ acquired just before bacteria inoculation (at time $t = 0$). We set to 0 all negative pixels of the resulting image. Third, we multiply, element by element, this matrix by the defined mask, i.e., $B_t = I(x, y)\, M(x, y)$, obtaining the local biomass distribution.

Pore space occupied by biomass (PS_B) and anoxic microenvironments (PS_N). The quantification of the pore space occupied by biomass is performed starting from the maps B_t. Each biomass map was transformed into a binary map $BinB_t$ by assigning 1 to all pixels with a value of $B_t > 0$. This means that we consider all pixels where light is scattered compared to the image at $t = 0$ as occupied by newly grown biomass. The value of PS_B is then computed as

$$PS_B = \frac{\Sigma BinB_t}{\Sigma M} 100 \tag{2}$$

Similarly, to identify anoxic microenvironments, the O_2 maps (c_{O_2}) were transformed into binary images $Binc_{O_2}$ by associating with the value of 1 all pixels where $c_{O_2} < TrO_2$ and 0

otherwise. The value of PS_N results from

$$PS_B = \frac{\Sigma Binc_{O_2}}{\Sigma M} 100 \tag{3}$$

S4: Details on the adjusted Pearson Correlation Coefficient

To quantitatively correlate the emergence of the microenvironments to the location of bacterial colonies, we compute an adjusted Pearson Correlation Coefficient (PCC), defined as

$$PCC(t) = \frac{\sum_{xy} \left((O_2^C(x,y) - E[O_2^C]) \left(B_t(x,y) - E[B_t](t) \right) \right)}{\sqrt{\sum_{xy} \left(O_2^C(x,y) - E[O_2^C] \right)^2 \sum_{xy} \left(B_t(x,y) - E[B_t](t) \right)^2}} \tag{4}$$

where the volume averages of biomass $E[B_t]$ was defined above and the complementary oxygen concentration O_2^C is defined as

$$O_2^C = 1 - \frac{\max(c_{O_2}) - c_{O_2}}{\max(c_{O_2})} \tag{5}$$

and $E[O_2^C]$ represents its overall average. The O_2^C spatial map gets values between 0 and 1, and is the complementary spatial map of the O_2 concentration being close to 0 for high oxygen values and close to 1 for low ones.

S5: Details on TrO_2 selection and results robustness

A universally shared definition of anoxic microenvironment has not been established yet, as discussed in section "Anoxic microenvironments are correlated to bacterial colony growth in space and time" of the manuscript. The metric TrO_2should be adjusted as a function of the strain/process and the environment one is interested in. In this work, we do not explore the activation of any facultative metabolism and, thus, such strain-specific threshold identification cannot be applied and we defined our threshold based on a purely statistical criterion. We have analyzed all oxygen concentration maps in terms of probability density function (*pdf*), average ($E[O_2]$) and standard deviation (σ). The maximum standard deviation, corresponding to the highest observed variance around the average value, occurs at 47 tPV in replicate 3 of our experiment and settles around 10% of the average value $E[O_2]$ (see Figure S4). Acknowledging a component of arbitrariness in the choice, we defined O_2 concentrations lower than $E[O_2]$-2σ to be significantly different from the bulk value, or, equivalently, set the threshold $TrO_2 = 0.8E[O_2]$. According to the chosen criterion, the anoxic microenvironments constitute 5^{th}-percentile of the *pdf* (see Figure S4). This criterion is then transferred to all the O_2 maps.

Still, the results proposed in the manuscript are invariant to chosen Tr_{O2}. We have tested the performance of the proposed metric $Da(\lambda)$ (accounting for colony morphology) and $Da(R_{EQ})$ (assuming round colonies) to identify anoxic microenvironment formation. We selected two more stringent TrO_2 in addition to $0.8E[O_2]$, i.e., $0.7E[O_2]$ and $0.6E[O_2]$. We assessed the improved predictability of anoxic microenvironment formation led by $Da(\lambda)$ compared to $Da(R_{EQ})$ using as criterion the rate of metric success. We define the latter as the percentage of data for which the observed $Colony\ O_2/Tr_{O_2}$ is correctly interpreted by the metrics $Da(\lambda)$ and $Da(R_{EQ})$, i.e., observed $Colony\ O_2/Tr_{O_2}$ <1 associated with Da >1 and *vice versa*. The comparison of performances of $Da(\lambda)$ and $Da(R_{EQ})$ (Table S.1) clearly indicate that the results presented in the manuscript are insensitive to the chosen Tr_{O2} and accounting for colony morphology provides a better interpretation of the anoxic

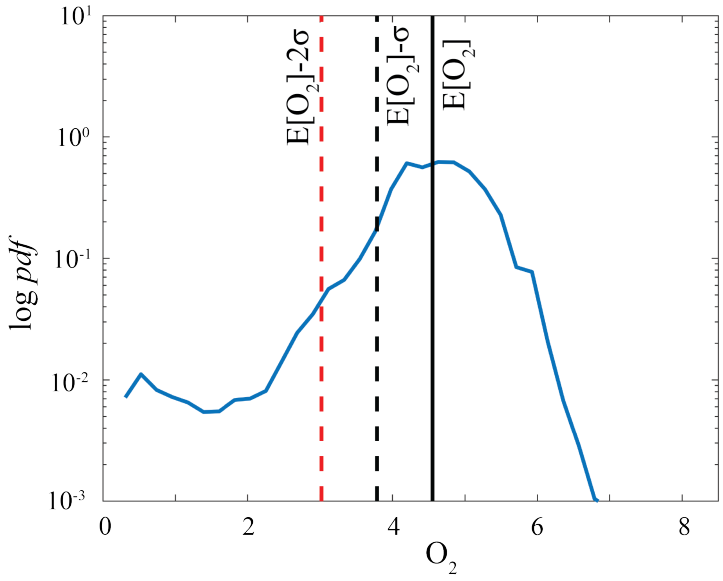

Figure S. 4: Probability density function *pdf* of O_2 concentrations at 47 tPV in replicate 3 of the experiment. Solid and dashed black lines indicate the average ($E[O_2]$) and the variability around the average value ($E[O_2] - \sigma$) of the *pdf*, respectively. The dashed red line is the chosen threshold for anoxic microenvironment identification.

microenvironment formation for all explored Tr_{O2}.

Table S. 1: Rate of success and failure of the metrics $Da(\lambda)$ and $Da(R_{EQ})$to predict the formation of anoxic microenvironments for different imposed Tr_{O2}.

Tr_{O2}	Rate of success [%]		Rate of failure [%]	
	$Da(\lambda)$	$Da(R_{EQ})$	$Da(\lambda)$	$Da(R_{EQ})$
$0.8E[O_2]$	96.5	65.6	3.5	34.4
$0.7E[O_2]$	98.5	66.5	1.5	33.5
$0.6E[O_2]$	98.2	66.6	1.8	33.4

S6: Additional results for the experiment with NOA-81 coated chip

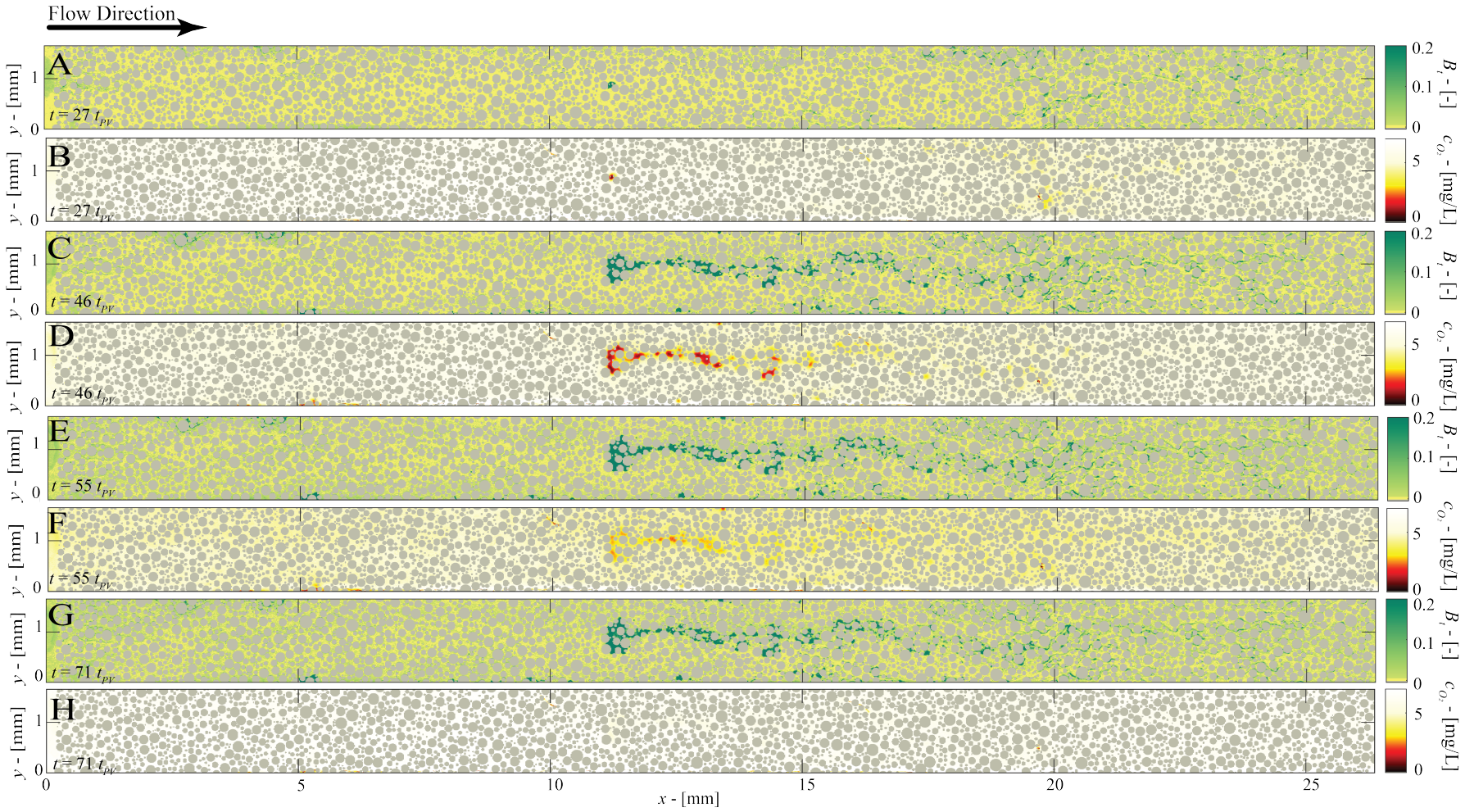

Figure S. 5: Spatial distribution of B_t for replicate 1 of the experiment with NOA-81 coated chip at $t = 27t_{PV}$ (panel A), $t = 46t_{PV}$ (panel C), $t = 55t_{PV}$ (panel E) and $t = 71t_{PV}$ (panel G) compared to the corresponding C_{O_2} maps ($t = 27t_{PV}$ in panel B, $t = 46t_{PV}$ in panel D, $t = 55t_{PV}$ in panel F, $t = 71t_{PV}$ in panel H).

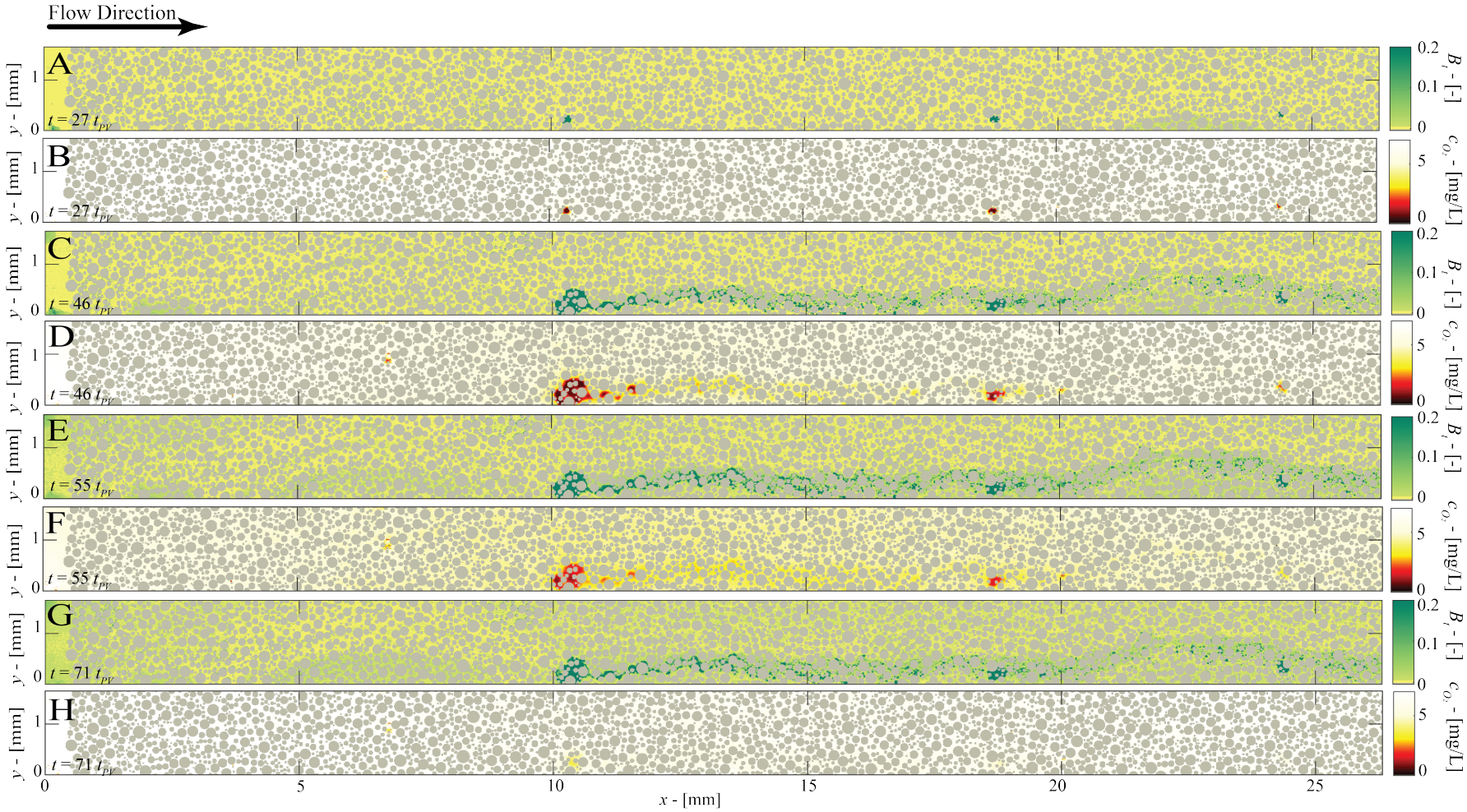

Figure S. 6: Spatial distribution of B_t for replicate 2 of the experiment with NOA-81 coated chip at $t = 27t_{PV}$ (panel A), $t = 46t_{PV}$ (panel C), $t = 55t_{PV}$ (panel E) and $t = 71t_{PV}$ (panel G) compared to the corresponding C_{O_2} maps ($t = 27t_{PV}$ in panel B, $t = 46t_{PV}$ in panel D, $t = 55t_{PV}$ in panel F, $t = 71t_{PV}$ in panel H).

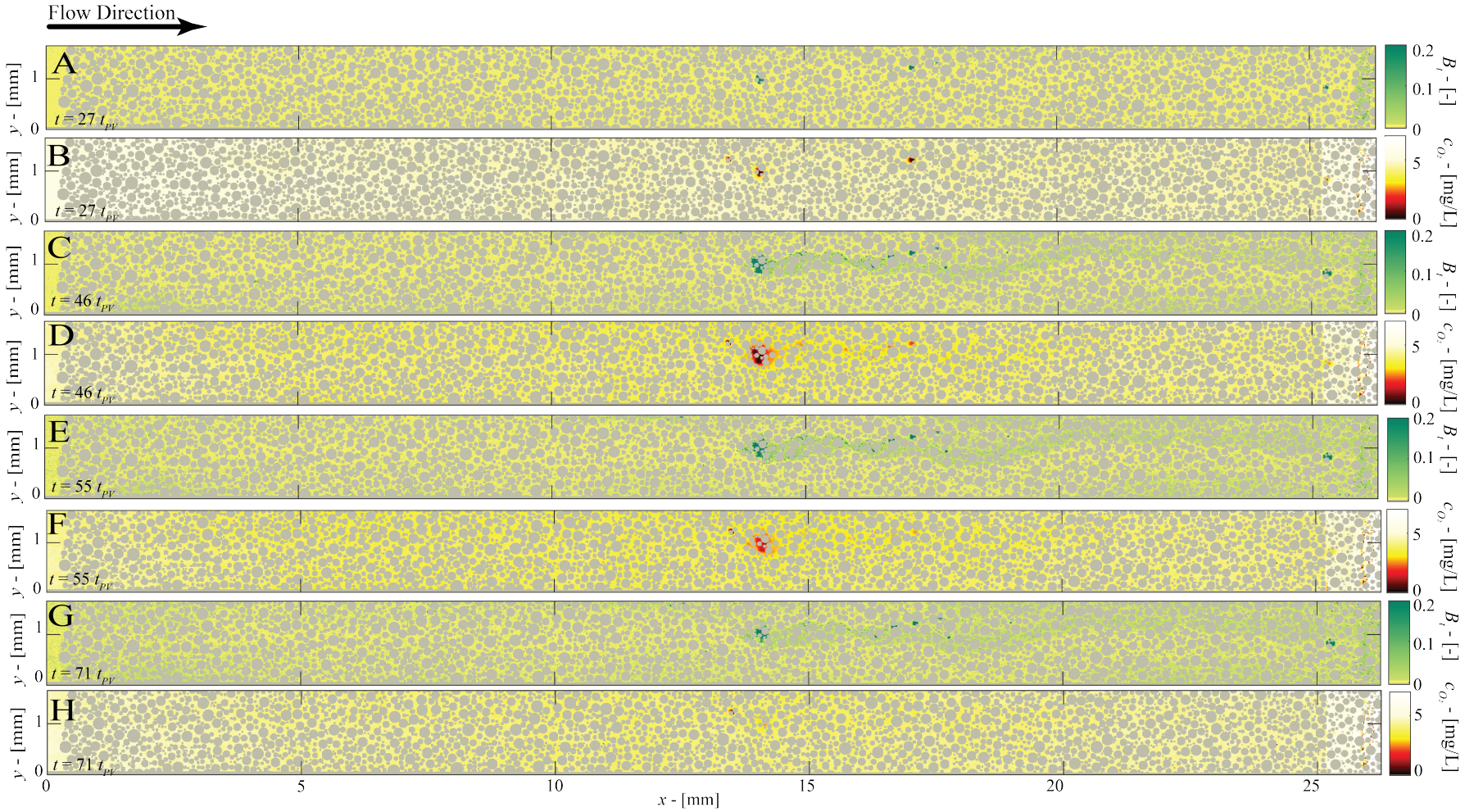

Figure S. 7: Spatial distribution of B_t for replicate 3 of the experiment with NOA-81 coated chip at $t = 27t_{PV}$ (panel A), $t = 46t_{PV}$ (panel C), $t = 55t_{PV}$ (panel E) and $t = 71t_{PV}$ (panel G) compared to the corresponding C_{O_2} maps ($t = 27t_{PV}$ in panel B, $t = 46t_{PV}$ in panel D, $t = 55t_{PV}$ in panel F, $t = 71t_{PV}$ in panel H).

S7: $Da(\lambda)$ time variability

In the manuscript, we present the data of $Da(\lambda)$ as an average between 27 and 55 t_{PV}, to capture the mean behavior of the colony in the time interval of interest, i.e., the one associated with anoxic microenvironment formation. We investigated the time variability of the $Da(\lambda)$ as a consequence of λ temporal behavior in Figure S.8 where the mean values presented in the main manuscript are enclosed in their range, i.e. between the maximum and minimum value observed in the time interval for each datum.

On the one hand, for $Colony\ O_2/Tr_{O_2} > 1.2$, all of the data and the corresponding ranges fall in $Da(\lambda) < 1$ indicating that, regardless the observation time, the conditions for the formation of anoxic microenvironments are never met. On the other hand, colonies that show on average a $Colony\ O_2/Tr_{O_2} < 0.9$ are characterized by a $Da(\lambda)$ that is always greater than one. This leads to the formation of microenvironments with highly depleted O_2 concentration in their core.

Finally, for $0.9 < Colony\ O_2/Tr_{O_2} < 1.2$, we observe a transition zone where the mean $Da(\lambda)$ and the associated range are progressively shifted towards higher values for decreasing level of average O_2 concentration. We can deduce that some colonies may have a fluctuating growth behavior in time and, thus, the conditions for the formation of anoxic microenvironments, as defined in our work, are not stably met. As a consequence, these colonies present an average $Colony\ O_2/Tr_{O_2}$ around one, i.e. close to the chosen threshold.

To conclude, the overall trend of $Da(\lambda)$ values and their associated temporal ranges is consistent with the observed O_2 average concentration, supporting the good performances of $Da(\lambda)$ as a metric for identifying the conditions for anoxic microenvironment formation.

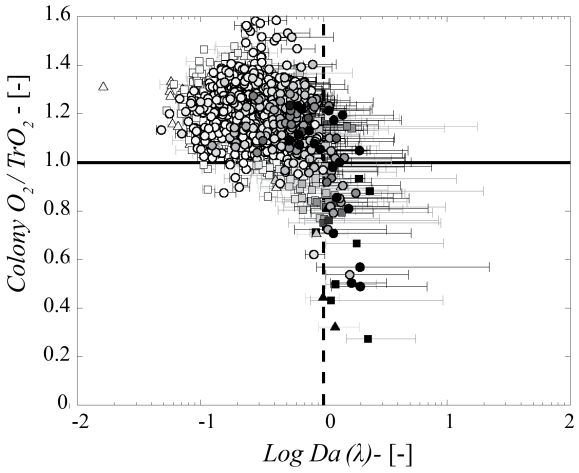

Figure S. 8: Behavior of Da computed for each biomass cluster using λ as O_2 diffusion characteristic length scale in as a function of the average value of O_2 measured inside each cluster for the control experiment without NOA-81 coated chip. Symbols represent the averaged value of $Da(\lambda)$ over the time interval between 27 and 55 t_{PV}, corresponding to what presented in the manuscript. The horizontal bars indicate the range associated with each point, i.e. the minimum and the maximum value observed in the time interval between 27 and 55 t_{PV}. The dashed vertical line highlights the $Da = 1$, while the horizontal solid line represents the threshold ($Colony\ O_2/Tr_{O_2}$) used to discriminate between a well-oxygenated and an anoxic colony. Markers face colors indicate the average A of the colony during the chosen interval of time.

S8: Results for uncoated chip - control scenario

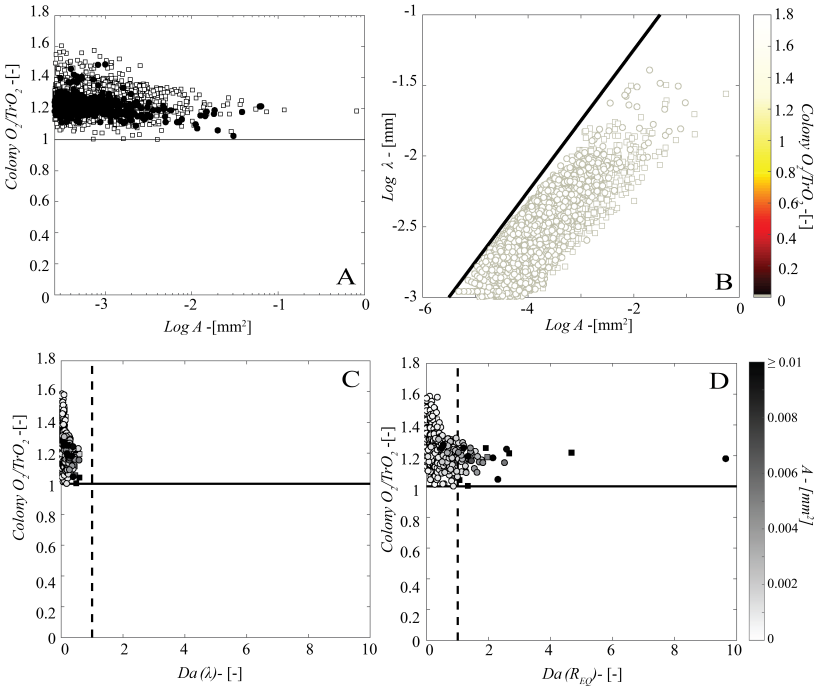

Figure S. 9: A) Values of the average oxygen level observed in each colony normalized to the threshold used for anoxic microenvironment identification ($Colony\ O_2/Tr_{O_2}$) as a function of the areas covered by each colony at 47 t_{PV}. B) Values of the characteristic colony length scales λ as a function of the colony area for the experiment without NOA-81 coating at 47 t_{PV}. Markers color indicates the average oxygen level observed in each colony normalized to the threshold used for anoxic microenvironment identification ($Colony\ O_2/Tr_{O_2}$). In both panels, circles and squares refer to replica 1 and replica 2 of the experiment. In panles C and D, behavior of the average value of Da computed for each biomass cluster using λ (panel C) and R_{EQ} (panel D) as O_2 diffusion characteristic length scale in R_T of Eq.**??** as a function of the average value of O_2 measured inside each cluster for the control experiment without NOA-81 coated chip. In both panels C and D, the $Da(\lambda)$ and $Da(R_{EQ})$, respectively, are averaged over the time interval between 27 and 55 t_{PV}, corresponding to what presented in the manuscript. The dashed vertical line highlights the $Da = 1$, while the horizontal solid line represents the threshold ($O_{2(A)/Tr_{O_2}}$) used to discriminate between a well-oxygenated and an anoxic colony. Markers face colors indicate the average A of the colony during the chosen interval of time.

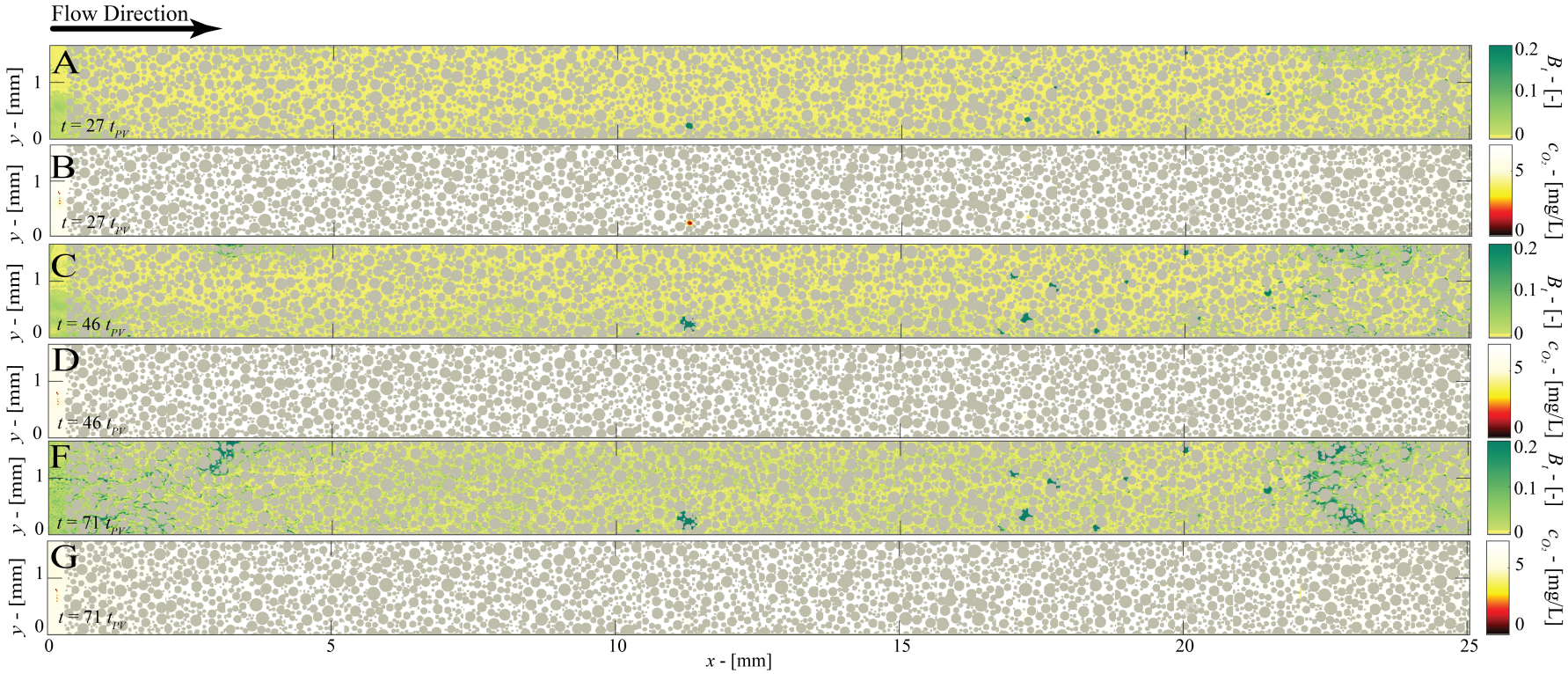

Figure S. 10: Spatial distribution of B for replicate 1 of the experiment with uncoated chip at $t = 27t_{PV}$ (panel A), $t = 46t_{PV}$ (panel C) and $t = 27t_{PV}$ (panel F) compared to the corresponding c_{O_2} maps ($t = 27t_{PV}$ in panel B, $t = 46t_{PV}$ in panel D, $t = 71t_{PV}$ in panel G).

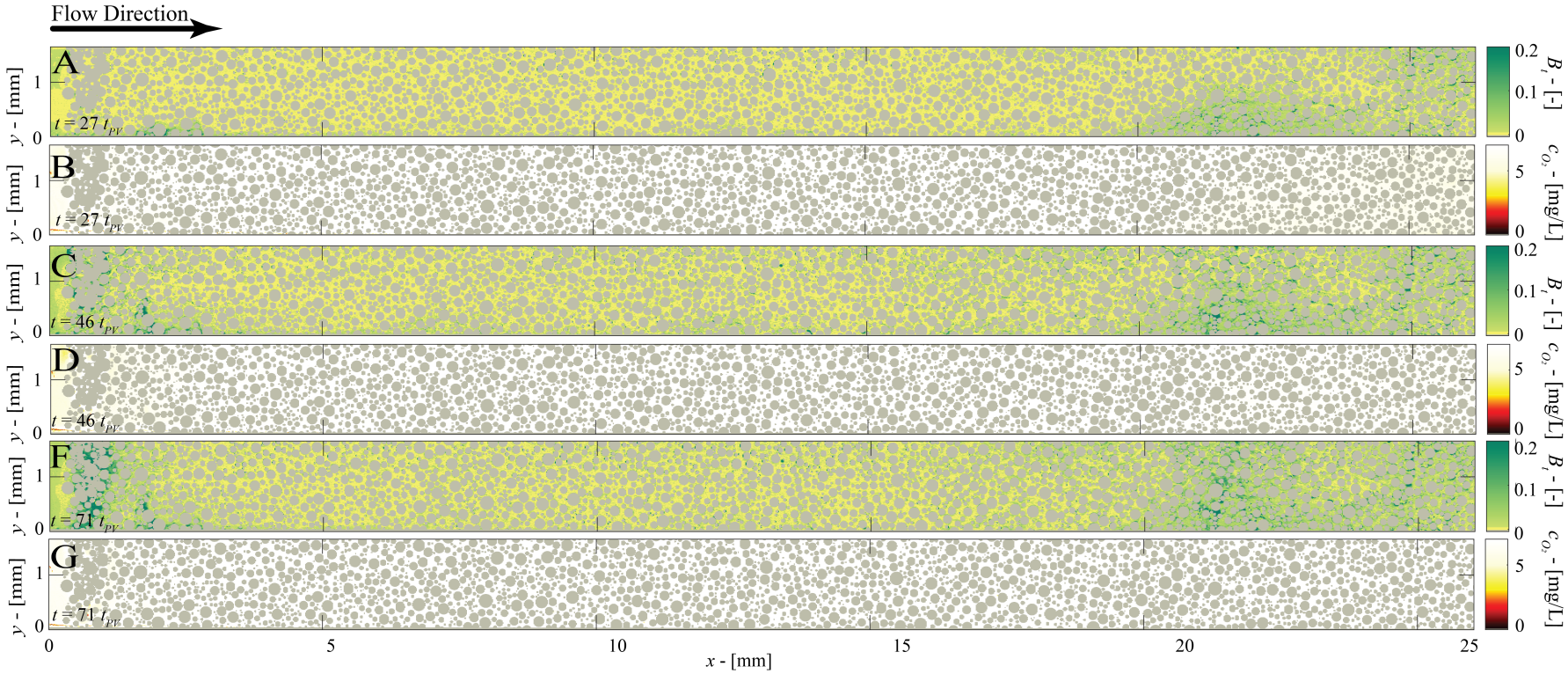

Figure S. 11: Spatial distribution of B for replicate 2 of the experiment with uncoated chip at $t = 27t_{PV}$ (panel A), $t = 46t_{PV}$ (panel C) and $t = 27t_{PV}$ (panel F) compared to the corresponding c_{O_2} maps ($t = 27t_{PV}$ in panel B, $t = 46t_{PV}$ in panel D, $t = 71t_{PV}$ in panel G)

References

[1] M. Moßhammer et al. ACS Sens. 2016, 1, 6, 681–687